

# **Ground-based Lidar Measurements of Aerosols During ACE-2: Instrument Description, Results, and Comparisons with other Ground-based and Airborne Measurements**

Ellsworth J. Welton <sup>1</sup>, Kenneth J. Voss <sup>1</sup>, Howard R. Gordon <sup>1</sup>, Hal Maring <sup>2</sup>,  
Alexander Smirnov <sup>3</sup>, Brent Holben <sup>4</sup>, Beat Schmid <sup>5</sup>, John M. Livingston <sup>6</sup>,  
Philip B. Russell <sup>7</sup>, Philip A. Durkee <sup>8</sup>, Paola Formenti <sup>9</sup>, Meinrat O. Andreae <sup>9</sup>

1. University of Miami, Physics Department, Miami, FL
2. University of Miami, Rosenstiel School of Marine and Atmospheric Science, Miami, FL
3. Science Systems and Applications, Inc. - NASA / GSFC, Greenbelt, MD
4. NASA / GSFC, Greenbelt, MD
5. Bay Area Environmental Research Institute, San Francisco, CA
6. SRI International, Menlo Park, CA
7. NASA Ames Research Center, Moffett Field, CA
8. Naval Postgraduate School, Monterey, CA
9. Max Planck Institute for Chemistry, Biogeochemistry Dept., PO 3060, 55020 Mainz,  
Germany

**Abstract:**

A micro-pulse lidar system (MPL) was used to measure the vertical and horizontal distribution of aerosols during the Aerosol Characterization Experiment 2 (ACE-2) in June and July of 1997. The MPL measurements were made at the Izaña observatory (IZO), a weather station located on a mountain ridge (28°18' N, 16°30' W, 2367 m asl) near the center of the island of Tenerife, Canary Islands. The MPL was used to acquire aerosol backscatter, extinction, and optical depth profiles at IZO. System tests and calibration procedures are discussed, and analysis of aerosol optical profiles acquired during ACE-2 are presented. The optical characterization of upslope aerosol layers normally present at IZO (the background aerosol), and of a Saharan dust episode during the middle of ACE-2, are presented. Comparisons of the MPL data with data from other co-located instruments are also presented. The comparisons showed good during both the clean, upslope period and the dust episode. Finally, results show the possible perturbation of the bottom of the dust layer by upslope winds from the mountain.

## **1. Introduction**

The Aerosol Characterization Experiment 2 (ACE-2) ran from June 16, 1997 to July 25, 1997. The purpose of ACE-2 was to study the radiative properties and physical characteristics of anthropogenic aerosols from Europe, and dust aerosols from Africa, as they are transported across the North Atlantic Ocean. An overview of ACE-2 operations and specific activities can be found in Raes et al. (this issue). One of the ACE-2 activities was the “clear sky column closure experiment” (CLEARCOLUMN) and was aimed at simultaneous measurements of aerosol properties using a variety of different platforms in order to assess the aerosol direct radiative forcing (Heintzenberg and Russell, this issue). The work presented in this paper was part of the CLEARCOLUMN effort during ACE-2.

This paper will focus on lidar measurements of the vertical and horizontal structure of aerosols surrounding the Izaña observatory (IZO) on Tenerife, Canary Islands during ACE-2. IZO is located on a mountain ridge (28°18' N, 16°30' W, 2367 m asl) near the center of the island and has often been used as a site for the study of various aerosol properties (Prospero et al., 1995; Raes et al., 1997; Smirnov et al., 1998). However, lidar measurements at IZO have not been made prior to this study. Thus, accurate knowledge of the spatial distribution of aerosols in the atmosphere surrounding IZO is needed in order to correctly apply the *in-situ* IZO data to studies of aerosols in the Eastern North Atlantic region. The lidar data are used to assess the vertical distribution and horizontal homogeneity of the aerosols in the atmosphere around IZO (10-30 km radius).

In addition to the lidar observations, *in-situ* aerosol mass concentration and extinction coefficient measurements were made at IZO. These *in-situ* measurements were used to aid in the calibration of the lidar system (as described in Section 3), and in comparisons with the near-IZO-range lidar data. Sunphotometer measurements were also made at IZO in order to supply spectral aerosol optical depth (AOD) measurements for CLEARCOLUMN efforts and for use in a lidar inversion algorithm (Appendix). The algorithm uses the sunphotometer AOD along with the lidar data to produce profiles of the

aerosol extinction coefficient and AOD, and the columnar backscatter-extinction ratio. The lidar derived aerosol optical data are used to show normal IZO site conditions, as well as conditions seen during Saharan dust passages. Finally, comparisons between the lidar data and data from other ACE-2 CLEARCOLUMN instruments are presented. In addition to daily comparisons with the other IZO instruments, joint measurements of the AOD on the afternoon of the July 17, 1997 dust episode were performed with the lidar, a sunphotometer on board an ACE-2 aircraft, and a radiometer installed on the nearby volcano of Tenerife (Teide). The comparisons demonstrate the success of the lidar calibration techniques and the lidar inversion algorithm, and show that lidar analysis can produce accurate profiles of ambient aerosol optical properties.

## **2. Instrumentation**

### **2.1 Micro-pulse Lidar System (MPL)**

The lidar used in this study is a micro-pulse lidar system (MPL) and is manufactured by Science & Engineering Services Inc., USA. Basic MPL design and background is described in Spinhirne (1993) and Spinhirne et al. (1995). The MPL system is revolutionary in that it uses rapidly pulsed low intensity laser light instead of slowly pulsed very high intensity laser light that has been used in previous lidar systems. The MPL system has  $\mu\text{J}$  output energies and the beam is expanded to 20.32 cm in diameter which achieves ANSI eye-safe standards. A pulse repetition frequency (PRF) of 2500 Hz allows the system to average many low energy pulses in a short time to achieve a good signal-to-noise ratio. In practice, an averaging time of 1 minute is used for data collection but the stored signals can be averaged over longer periods if necessary during post-analysis. The MPL system also has a high vertical spatial resolution (75 m is used with the MPL system in this study). Finally, the MPL system is small compared to previous lidar

systems and is therefore much more portable than its predecessors. The small size of the MPL system allows the operator to perform lidar measurements at any zenith angle by carefully tilting the instrument to the desired angle. It is therefore possible to perform horizontal and slant path measurements with the MPL as well as the normal vertical measurements. Care must be taken when operating the MPL during sunny days as direct sunlight entering the MPL can cause serious damage to the detector. The MPL must be tilted away from the sun or turned off and covered in such conditions.

The MPL is pictured schematically in Figure 1. The MPL transmitter-receiver (T-R) is located inside the climate housing and consists of a black 20.32 cm diameter cassegrain telescope with optics and electronics mounted directly below the telescope. The laser supply and scalar (data binning unit) are connected to the T-R, and along with the control computer, they must be located inside a separate climate controlled environment. The laser supply contains a diode pumped Nd:YLF laser with a fundamental pulse output wavelength of 1046 nm that is converted to 523 nm for lidar use after passage through a frequency doubling crystal. The MPL system used in this study was operated at the full laser power supply setting of 1 W. The pulse duration is 10 ns with a PRF of 2500 Hz and output energies ranging from 1 to 6  $\mu$ J depending upon system performance. Signals are received using the same telescope and are recorded with a Geiger mode avalanche photodiode.

The signals are stored as photons/sec (ph/sec). Since the receiver is a telescope focused at infinity, the T-R has difficulty accurately imaging near-range signals onto the detector. This problem is referred to as overlap error and causes the near-range signals (0 to approximately 2 km) to rapidly fall off in intensity the closer they are to the T-R. Since the majority of aerosols are contained in the first several kilometers of the atmosphere (or as at IZO, the first several kilometers in range from IZO), the overlap problem must be overcome. The procedures used in this study to correct for the MPL overlap are discussed in Section 3. The signals are binned in the scalar according to their time-of-flight from

transmission to signal reception and correspond to steps of 75 m in range. Our MPL system has a pause of approximately 1  $\mu$ s from activation of the detector to emission of the laser pulse. Thus, we disregard the first two signal bins and re-zero the range such that the third signal bin represents the signal return from 75 m.

A control computer is connected to the scalar and is used to control lidar operation, to visualize real-time lidar output, and to store the resulting lidar data. The data are stored in 1 hour binary files with each record containing a header followed by the signal in ph/sec at the successive 75 m increments up to a preset range (30 km). The maximum MPL range having usable data typically varies from approximately 30 km at night to about 10 km during reasonably clear daytime conditions. The lidar signals stored on the control computer contain background noise that is present from laser-detector crosstalk (afterpulse) and sunlight at 523 nm. Afterpulse noise must be corrected in post-analysis and the procedure is discussed in Section 3. Background sunlight noise is measured by the MPL in real time by measuring the detector signal after the maximum altitude signal (30 km) has arrived and before the next pulse is fired. This background signal is stored and used to correct the final signal by subtracting its value from each binned signal in post-analysis. The header information contains the time, output pulse energy, instrument temperatures, background sunlight energies, and information necessary for the operator to determine the altitude resolution used for each record in the data file.

## **2.2 Other IZO Instruments**

*In-situ* aerosol measurements were made at IZO. Aerosol mass concentration measurements were made with a Rupprecht & Patashnick Model 1400a tapered element oscillating microbalance and extinction coefficients were obtained with a Radiance Research particle/soot absorption photometer, a TSI Model 3563 integrating nephelometer, and a Radiance Research Model M903 integrating nephelometer. The IZO *in-situ* measurements were used for MPL calibrations and in comparisons with the MPL. A NASA AERONET

cimel sunphotometer (Holben et al., 1998) was also operated at IZO for the duration of ACE-2. The cimel was used to acquire independent measurements of the AOD (Smirnov et al., 1998) for input to the lidar inversion algorithm (Appendix) and to perform aerosol measurements specific to AERONET and CLEARCOLUMN operations.

### **2.3 Airborne and Teide Instruments**

The MPL was used to supply morning lidar signal profiles via fax to ACE-2 headquarters to assist in the pre-flight briefing for the Center for Interdisciplinary Remotely Piloted Aircraft Studies Pelican aircraft, which was one of the aircraft participating in ACE-2. AOD measurements were made on-board the Pelican with the NASA Ames Airborne Tracking 14-channel Sunphotometer, AATS-14, (Schmid et al., this issue). AOD measurements were also made on the island's volcano, Teide (28°16' N, 16°36' W, 3570 m asl), during ACE-2 using a multi-filter rotating shadowband radiometer (Formenti et al., 1998; Formenti et al., this issue). AOD data acquired with the AATS-14 and the shadowband are used in the comparison on July 17, 1997.

## **3. The Lidar Equation and MPL Calibrations**

The basic lidar equation for returned signals is given by

$$S_L(z) = \frac{CE}{(z - z_L)^2} [R_R(z) + R_A(z)] \exp -2 \int_{z_L}^z (R_R(z) + R_A(z)) dz \quad (1)$$

where  $S_L(z)$  is the lidar signal at altitude  $z$  (m),  $C$  is the system constant (principally a function of the optics),  $E$  is the output energy in  $\mu\text{J}$ ,  $z_L$  is the lidar altitude (m),  $R_R(z)$  and  $R_A(z)$  are the backscatter ( $\text{m}^{-1} \text{sr}^{-1}$ ) and extinction ( $\text{m}^{-1}$ ) coefficients respectively, the  $R$  subscript denotes a Rayleigh quantity (due to molecular scattering), and the  $A$  subscript denotes an aerosol quantity.

The backscatter coefficient is related to extinction by

$$S_r(z) = R(z) S_o(z), \quad (2)$$

where  $R(z)$  is the backscatter-extinction ratio (BER) with units of  $\text{sr}^{-1}$ . The aerosol BER is considered to be constant for each profile in this study and thus is referred to as the columnar backscatter-extinction ratio,  $R_A$ . The BER is related to the aerosol phase function,  $P_A(\theta)$  (normalized to 4  $\pi$ ), and the single scattering albedo,  $\omega_o$ , by  $4\pi \cdot R_A = \omega_o P_A(\theta)$ .

It is useful to rewrite Eq. (1) by multiplying by the range squared,  $(z-z_L)^2$ , to remove the range dependent fall off in the signal returns and to use the BER to rewrite the equation in terms of only the backscatter coefficient,

$$S_r(z) = CE [R_R(z) + R_A(z)] \exp \left[ -\frac{2}{R_R} \int_{z_L}^z R_R(z) dz \right] \exp \left[ -\frac{2}{R_A} \int_{z_L}^z R_A(z) dz \right] \quad (3)$$

where  $S_r(z)$  is referred to as the range-corrected lidar signal,  $R_R$  is the BER for Rayleigh scattering, and  $R_A$  is the BER for the aerosols. The lidar equation must be solved for the unknown aerosol quantities,  $R_A(z)$ ,  $S_o(z)$ , and  $R_A$ . The Rayleigh optical functions are constructed using data from Hansen and Travis (1974). The BER values used above are assumed to be constant with altitude. While  $R_R$  is constant,  $R_A$  may actually vary. Algorithms exist for lidar analysis using altitude dependent  $R_A$  values (Klett, 1985; Kovalev, 1993) but require additional assumptions or measurements of the vertical structure of the aerosol optical properties that were not possible for this work. The lidar inversion algorithm in this study uses an independent AOD measurement to iterate a basic lidar inversion (Fernald et al., 1984) to produce the  $S_o(z)$  and  $R_A(z)$  profiles, and to calculate the value of  $R_A$ . The lidar inversion algorithm used in this study is discussed in the Appendix. Errors related to assuming constant BER values are also addressed in the Appendix.



The above discussion relates to vertical lidar measurements. Horizontal lidar measurements are used to assess the horizontal homogeneity of the atmosphere at a particular altitude. The backscatter and extinction coefficients for a horizontal lidar measurement during conditions of horizontal homogeneity are constant by definition. Therefore, a horizontal lidar signal simplifies Eq. (3) to

$$S_H(x) = CE [ \beta_R(z_L) + \beta_A(z_L) ] \exp \left[ -2 \left( \gamma_R(z_L) + \gamma_A(z_L) \right) x \right], \quad (4)$$

where  $S_H(x)$  is the horizontal lidar signal,  $x$  is the horizontal range in m, and the values of  $\beta_i(z_L)$  and  $\gamma_i(z_L)$  are constants with respect to  $x$ . Furthermore, taking the natural logarithm of both sides of Eq. (4) gives

$$\ln[S_H(x)] = -2 \left[ \gamma_R(z_L) + \gamma_A(z_L) \right] x + \ln \left[ CE \left( \beta_R(z_L) + \beta_A(z_L) \right) \right]. \quad (5)$$

Thus, the slope of  $\ln[S_H(x)]$  versus the range  $x$  yields  $-2 \gamma_{\text{total}}$  and the y-intercept is  $\ln[CE \gamma_{\text{total}}]$  for the horizontal homogeneous case. If the atmosphere is not horizontally homogeneous at the lidar altitude, then a horizontal lidar plot of  $\ln[S_r(z)]$  versus the range  $x$  will not produce a straight line.

### MPL Calibration Procedure

Equation (3) is an ideal lidar signal. Actual lidar signals are effected by both afterpulse and overlap problems as mentioned in Section 2. Thus, an actual MPL range-corrected signal is given by

$$S_r(z) = C O(z) E \left[ \beta_R(z) + \beta_A(z) \right] \exp \left[ -\frac{2}{R_R} \int_{z_L}^z \beta_R(z) dz \right] \exp \left[ -\frac{2}{R_A} \int_{z_L}^z \beta_A(z) dz \right] + A(z) \quad (6)$$

where  $O(z)$  and  $A(z)$  represent the overlap and afterpulse functions.

Calibration of the MPL system involves correcting for the afterpulse and overlap functions. Additionally, lidar calibration can also involve determination of the lidar system

constant,  $C$ . However, the determination of the system constant was not a focus of this study since it is not needed to produce the optical coefficient profiles when the AOD is measured by an independent instrument (Appendix).

The calibration procedures applied to the MPL during ACE-2 differ from the normal MPL calibration techniques (Welton, 1998). The laser frequency doubling crystal in the MPL system burned midway through ACE-2. The cause of the burned crystal was attributed to a poor ground connection between the laser temperature controller on the laser supply and the laser itself, located inside the T-R. Data continued to be taken with the MPL system because the problem was not noticed until the end of the experiment.

The data acquired after the crystal burn had noticeable effects caused by signal loss and diffraction from the burn pattern. Signal loss resulted from light scattered off axis, by the hole, that was lost before reaching the T-R. Diffraction effects were believed to be the cause of distortions in the outgoing laser pulses. These diffraction effects caused distortion of the MPL overlap characteristics and altered the afterpulse signal. These problems became worse as the experiment continued. Thus it was not possible to use the pre-experiment calibrations or post-calibrations to correct the entire data set taken during the experiment. Therefore, a new lidar calibration procedure was developed to handle the MPL data during ACE-2. The procedure is based on normalization of the MPL signals to those signals from a molecular (Rayleigh) only atmosphere and is described below.

Due to its unique location, IZO is in the free troposphere at night (Raes et al., 1997). The MPL performed vertical profile measurements during normal ACE-2 nighttime lidar operations. Several nights were very clean and the lidar returns were assumed to represent pure Rayleigh scattering with the exception of the afterpulse and overlap effects. This assumption was based on normal nighttime conditions and inspection of both aerosol mass concentration and aerosol extinction coefficient measurements made at the observatory during the night. The early mornings (00:00 GMT to 03:00 GMT) of June 29

and July 15, 1997 were chosen as having clean (negligible aerosol concentrations) based on the low aerosol concentrations and extinction coefficients shown in Figures 2a and 2b.

At 00:00, 01:00, 02:00, and 03:00 GMT, a 15 minute average Rayleigh lidar signal,  $S_R(z)$ , was calculated using Eq. (3) with  $A(z) = 0$ ,  $E$  obtained from the actual time corresponding measured lidar signal, and with  $C$  set equal to 100,

$$S_R(z) = 100E_R(z) \exp \left[ -\frac{2}{R_R} \int_{z_L}^z R_R(z) dz \right] . \quad (7)$$

The actual measured lidar signals are expressed using the following equation,

$$S_L(z) = CE O(z) R_R(z) \exp \left[ -\frac{2}{R_R} \int_{z_L}^z R_R(z) dz \right] + A(z) , \quad (8)$$

where  $A(z)$  is still assumed to be zero. Eq. (8) can be rewritten in terms of the Rayleigh-only signal as

$$S_L(z) = O(z)S_R(z) + A(z) . \quad (9)$$

The term  $S_R(z)$  is calculated and the term  $S_L(z)$  is measured with the MPL system, thus the only unknowns in Eq. (9) are  $O(z)$  and  $A(z)$ . A linear regression was performed using Eq. (9), the calculated Rayleigh signal, and the measured lidar signal for each altitude bin in each period (4 each night) from the chosen nights. The y intercepts were used to construct the afterpulse function and the slope was used to determine the overlap function. The resulting overlap and afterpulse functions are shown in Figures 3a and 3b.

The overlap function for June 29 approaches an asymptote of almost 10, instead of the usual value of 1, as the range increases beyond 2 km. This is due to setting  $C$  equal to 100 for the calibration procedure. The actual value of  $C$  for the June 29 period was most likely much higher than 100. This is also the reason for the negative afterpulse values calculated for June 29. The overlap and afterpulse functions for June 29 do not represent the physical overlap and afterpulse values for this period due to the arbitrary choice of  $C$ .

However, the overlap and afterpulse functions still produce the correct lidar calibration. Also, the MPL crystal problems increased in magnitude as the experiment progressed, and the value of  $C$  decreased significantly. The value of  $C$  was very close to 100 by July 15, as evidenced by the overlap asymptotic limit of approximately 1 for this day. Also, the afterpulse values for July 15 are similar to those obtained using the MPL with no crystal problem (Welton, 1998).

The overlap and afterpulse functions were used to correct MPL signals only during the days immediately after the calibration night. As an example of applying the calibration functions to the MPL data, Figure 4 shows the original lidar signal measured at 00:00 GMT on June 30, the calculated Rayleigh signal, and the corresponding overlap and afterpulse corrected signal. The signal now resembles a free troposphere Rayleigh-only lidar signal and demonstrates the success of the calibration procedure.

#### **4. Analysis of ACE-2 MPL Data**

The MPL was operated on a daily schedule that involved vertical, horizontal, and slant path (T-R tilted to 60° zenith angle) measurements at specific times of the day. Vertical measurements were typically performed from 00:00 GMT to 10:30 GMT and again from 16:30 GMT to 23:59 GMT each day. Horizontal measurements were usually performed from 10:30 GMT to 11:00 GMT and from 16:00 GMT to 16:30 GMT, and slant path measurements were made each day from 11:00 GMT to 16:00 GMT. Slant path rather than vertical orientation was necessary during mid-day to prevent direct sunlight from entering the T-R and damaging the MPL detector and optics. The schedule was occasionally altered to accommodate Pelican overflights and special ACE-2 directed activities. For this study, only vertical and selected horizontal measurements are discussed.

MPL installation and testing was performed during the first weeks and normal operation began on June 28. The instrument problems with the MPL system became

substantial after July 20, 1997 and the resulting data from the correction procedure were not considered reliable. Thus, only MPL data from June 28 to July 20 were analyzed for this study. The MPL signals were calibrated using the procedure discussed in Section 3. The signals were then divided by the lidar constant  $C$  (set equal to 100) and the corresponding output energy  $E$ . The resulting profile is referred to as an attenuated backscatter signal (ABS, units of  $\text{m}^{-1} \text{sr}^{-1}$ ) because it is a profile of the total backscatter coefficient and is attenuated by the exponential transmission function. The ABS profiles for all the vertical measurements made from June 28 to July 20 showed that no aerosols were present above an altitude of approximately 6 km during ACE-2. Also, most days during ACE-2 produced similar ABS profiles and were identified as the normal site condition influenced by upslope aerosols. The periods, July 7 to July 9, and July 16 to July 18, showed much higher ABS values relative to the normal site profiles. These two periods correspond to the first and second Saharan dust passages observed during ACE-2. This study will focus on the normal upslope aerosol conditions at IZO during June 29 to July 1, and the Saharan dust episode from July 16 to July 18.

#### **4.1 Analysis of Upslope Aerosols**

During the day, local heating near IZO (along the mountain ridge) creates an upslope wind. This local wind carries aerosols from within the marine boundary layer (MBL) below IZO, to the level of IZO and beyond. The upslope aerosols appear in the early morning as the sun rises and subside by the late afternoon as the sun sets and the air temperature stabilizes. The presence of upslope aerosols during the daytime is characteristic of normal conditions at the IZO site (Raes et al., 1997), therefore, it is necessary to understand the upslope aerosol's spatial distribution and optical profile before analysis of the Saharan dust layers can be attempted.

Time series ABS profiles are shown for June 29 to July 1 in Figure 5. Also, ABS profiles from early morning to late afternoon on June 29 are shown in Figures 6a and 6b.

The ABS profile at 06:15 GMT, approximately 45 minutes before sunrise (~ 07:00 GMT) is representative of a Rayleigh-only profile, no aerosol layers are present. However, the profile at 07:15 GMT shows a weak aerosol layer extending to under 6 km in altitude. The profiles at 10:15 GMT and 17:15 GMT also show aerosol layers extending to under 6 km in altitude but with much higher ABS values just over IZO. These mid-day ABS profiles are significantly less than the earlier ABS profiles at higher altitudes due to the attenuation of the upslope layer. The ABS profile at 19:15 GMT shows the aerosol layer subsiding, with ABS values similar to the 07:15 GMT profile, and lower than during mid-day. Finally, the ABS profile at 22:15 GMT shows no indication of aerosol layers, and instead resembles the Rayleigh-only ABS profile at 06:15 GMT. The ABS profiles in Figures 6a and 6b clearly show the presence of the upslope aerosols and this pattern is typical for normal upslope conditions at IZO during ACE-2.

### **Upslope Aerosol Extinction Coefficient and Optical Depth Profiles**

The AOD measured with the IZO cimel was used to calculate the aerosol extinction coefficient (AEC), the columnar backscatter-extinction ratio (BER), and AOD profiles for the upslope aerosol layers on June 29, 1997 using the inversion algorithm discussed in the Appendix. The profiles shown for June 29 are representative of normal upslope aerosol conditions during ACE-2. The lidar AEC profiles are shown in Figure 7a and the AOD profiles are shown in Figure 7b. The daytime average AEC measured at IZO using the nephelometer is also shown in Figure 7a, and the AOD measured by the Teide shadowband is displayed in Figure 7b. The Rayleigh extinction coefficient profile is shown in Figure 7a for comparison.

Significant AEC values (greater than the Rayleigh extinction coefficient) extend from just under 3 km to approximately 3.5 km in altitude for the 08:15, 17:15, and 18:15 GMT profiles. The bottom of the upslope layer is lower during the late morning profile at 10:15 GMT and at this time the layer extends from approximately 2.5 km to 3.5 km in

altitude. The upslope layers at IZO typically begin forming at approximately 07:00 to 08:00 GMT and begin dissipating just prior to 18:00 GMT. The formation of the upslope aerosols corresponds with a gradual lowering of the bottom of the layer through to the late morning, and the dissipation of the upslope aerosols corresponds with a gradual increase in the altitude of the bottom of the layer.

The peak upslope aerosol AEC values are approximately  $1.5\text{e-}5\text{ m}^{-1}$ . These are not large compared with boundary layer values (Schmid et al., this issue) but are higher than free-troposphere values (Rayleigh values). The AEC values peak at approximately 3 km in altitude, but are much lower near IZO throughout the day. In order to check that this was not due to a poor calibration of the MPL, the nearest range lidar AEC value (2.442 km) was compared to the daytime (07:00 to 19:00 GMT) AEC measured at IZO using a nephelometer. The average lidar AEC value at 2.442 km for the 10:15 and 17:15 GMT profiles is  $4.4\text{e-}6\text{ m}^{-1}$ , which agrees well with the IZO nephelometer AEC value of  $\sim 5\text{e-}6\text{ m}^{-1}$ . However, the 08:15 and 18:15 GMT lidar AEC values (at 2.442 km) are much lower than the IZO value. This is most likely due to the rapidly changing aerosol conditions during the formation and dissipation of the upslope layer. The changing aerosol conditions (thus, varying AOD values from the cimel) and overall low AEC values, results in poorer inversion results.

The AOD measured with the Teide shadowband is compared to the lidar AOD value at 3.57 km in Figure 7b. The low AOD values measured by all instruments demonstrate the absence of Saharan dust during this period. The lidar AOD value at 3.57 km is approximately half of the Teide AOD value. The AOD values from both instruments are small and the difference between the two are within the bounds of measurement error. The difference in AOD may also be due to the presence of upslope aerosols specific to Teide which are not present one kilometer over IZO.

### **Upslope Aerosol Backscatter-Extinction Ratios**

The AEC and AOD profiles shown in Figures 7a and 7b each correspond to a calculated columnar BER value from the lidar inversion. The BER values for the 08:15, 10:15, 17:15, and 18:15 GMT profiles on June 29 are 0.018, 0.038, 0.031, and 0.017  $\text{sr}^{-1}$  respectively. Low BER values ( $\sim 0.020$ ) during the early morning and late afternoon, and higher BER values ( $\sim 0.035$ ) during mid-day were characteristic of upslope aerosol conditions at IZO during ACE-2. The low BER value of  $\sim 0.020$  occurs during the formation and dissipation of the upslope aerosol layer, while the higher BER value of  $\sim 0.035$  occurs during the stable mid-day period of the upslope layer.

The lidar  ${}_0P_A(\theta)$  value for the early morning and late afternoon periods averages  $\sim 0.25 \text{ sr}^{-1}$ , and averages  $\sim 0.44 \text{ sr}^{-1}$  for the mid-day period. Phase functions derived from the cimel during ACE-2 were generated using Mie theory (O. Dubovik, personal communication) and were used in conjunction with the lidar  ${}_0P_A(\theta)$  values in order to assess the impact of particle non-sphericity. The lidar BER values, and hence the lidar  ${}_0P_A(\theta)$  values, calculated using the lidar inversion algorithm in the Appendix are not dependent upon Mie theory and are direct calculations. Mishchenko et al. (1997) have shown that there are unique differences in the aerosol phase function for the ratio of non-spherical to spherical measurements. They have shown that, in general, there is little difference at forward scattering angles ( $0^\circ$  to  $10^\circ$ ), but that when particle non-sphericity is taken into account increased side-scattering (near  $120^\circ$ ) and decreased backscatter (at  $180^\circ$ ) occurs relative to spherical particle calculations. The data shown in Plate 5 of Mishchenko et al. (1997) depicts the behavior of both Mie and non-spherical phase functions for different size parameters,  $x_{\text{eff}}$ , using a refractive index of  $1.53 + 0.008i$ .

The cimel (henceforth referred to as Mie) phase functions at  $0^\circ$  and  $180^\circ$  and the lidar  ${}_0P_A(\theta)$  values (no Mie dependence) were used to determine the degree of particle



non-sphericity and a value of  $x_{\text{eff}}$  by comparison with the Plate 5 Mishchenko et al. (1997) data. The Mie phase functions at  $0^\circ$  are just over  $30 \text{ sr}^{-1}$  in the early morning (07:50 GMT) and from 70 to  $90 \text{ sr}^{-1}$  at mid-day (measurements at 11:00 and 17:30 GMT). The Mie phase functions at  $180^\circ$  are approximately  $0.3 \text{ sr}^{-1}$  in the early morning, and average approximately  $0.4 \text{ sr}^{-1}$  during mid-day. The forward and backward Mie phase function values given above do not exactly match the behavior of Mie functions in Plate 5 of Mishchenko et al. (1997) most likely due to differences in the refractive indices used to generate them. However, the ratio of the lidar to Mie phase function values still yields useful information. Comparing the forward Mie phase function values from the cimel with those given in Plate 5 of Mishchenko et al. (1997) give  $x_{\text{eff}}$  ranges from 6 to 10, which correspond to  $r_{\text{eff}}$  values from 0.5 to 0.8 microns using the lidar wavelength. The Mie phase functions at  $180^\circ$  are not much different from the lidar  ${}_0P_A(\ )$  values for morning and mid-day. The lidar  $P_A(\ )$  and Mie  $P_A(\ )$  values would then agree very well assuming  ${}_0$  is not significantly less than 1, indicating that the particles are fairly spherical in shape.

### **Upslope Horizontal Lidar Signal Results**

Analysis of horizontally aimed lidar measurements (approximately due East) during upslope conditions was performed. The natural logarithm of the horizontal ABS at 10:45 GMT on June 29 is shown in Figure 8 along with a calculated Rayleigh horizontal plot. The presence of the upslope aerosols along the side of the mountain is shown by the elevated and non-linear ABS values out to approximately 1.5 km from the side of the mountain. The plot becomes linear after 1.5 km, thus, the atmosphere does appear to be horizontally homogeneous from 1.5 km out to 6 km (the maximum daytime range of the MPL during most of ACE-2). However, near the side of the mountain, and near IZO, horizontal homogeneity does not exist due to the presence of the upslope aerosols.

## **4.2 Analysis of Saharan Dust Episode**

Three Saharan dust episodes occurred during ACE-2. Each episode was characterized by the presence of dust layers at and above the IZO site. The first dust episode started at mid-day on July 7 and continued until the afternoon of July 9. The second dust episode started late in the evening on July 16 and continued until the morning of July 18. The last dust episode started on the morning of July 25 and continued into July 26, past the end of ACE-2.

During much of the first dust episode, the MPL was orientated in the slant path position. During this episode, inspection of the dust layer lidar returns and IZO aerosol concentration and nephelometer data showed that very little of the dust was at the IZO altitude. The decision was made to orient the MPL on a slant path in order to attempt to measure dust data lower than the MPL's lowest vertical measurement range (75 m). As a result, there is little vertical MPL data during the first dust episode. Also, the last dust episode occurred after the period when the MPL data could be accurately corrected. Therefore, no usable MPL data exists for the last dust episode. The results presented below for Saharan dust layers are derived from analysis performed on data acquired during the second dust episode, from July 16 to July 18.

It is important to note that sulfates and other aerosol species have often been correlated with dust episodes at IZO and elsewhere over the North Atlantic Ocean (Welton et al., unpublished data; Maring, personal communication). Therefore, the results presented in this section for dust conditions at IZO are likely to include some effects from aerosols other than dust, and may in fact underestimate the effects of the dust aerosols alone.

A time series of ABS profiles from July 16 through July 18 is shown in Figure 9. The calibration of the MPL was more difficult for this period, relative to June 29, because the MPL crystal problems were much worse than in late June. The final July 16 to July 18 calibrated lidar data contains more noise than the June 29 to July 1 data. The straight lines running across the figure are due to noise in the calibrations and not aerosol effects. The

problem is only significant during mid-day at altitudes over 6 km (which exceeds the maximum aerosol altitude observed during ACE-2 using the MPL). This was due to a low signal-noise ratio caused by background sunlight and very high dust concentrations, corresponding to high signal attenuation, during mid-day.

The temporal extent of the dust layer is clearly evident. The dust layer appeared at approximately 22:00 GMT on July 16 at an altitude of approximately 3.5 km. The layer dropped in altitude by the morning of July 17 with the majority of the dust at altitudes from about 2.5 km to about 4 km until the late afternoon. The layer thickness narrowed in altitude considerably after 18:00 GMT on July 17. Most of the dust remained at altitudes from about 2.75 km to 3.5 km for the duration of the episode, which ended the morning of July 18.

### **Dust Aerosol Extinction Coefficient and Optical Depth Profiles**

The AOD measured with the IZO cimel was used to calculate the AEC, the columnar BER, and the AOD profiles for the dust layers on July 17, 1997 using the inversion algorithm discussed in the Appendix. The lidar AEC profiles calculated throughout the day (08:15, 10:15, 17:15, and 18:45 GMT) on July 17 are shown in Figure 10 along with the Rayleigh extinction coefficient profile for comparison. The AEC values for July 17 are orders of magnitude higher than the upslope values on June 29 and thus the presence of the dust is obvious. The peak AEC values were between  $1.5\text{e-}4$  and  $2\text{e-}4 \text{ m}^{-1}$  and were located just above 3 km in altitude. Significant AEC values (greater than the Rayleigh extinction coefficient) were present from the IZO altitude to just under 5 km.

The inversion results for 10:15 GMT and 17:15 GMT are slightly effected by the calibration noise problem discussed above. The signals are too noisy to start the inversion at 5 km or higher for these two times. Thus, the inversions were started at 4.8 and 4.5 km for the two profiles respectively. The end result is a profile which has fairly accurate AEC and AOD values due to the high concentrations of aerosol, but may have less accurate BER

values. The results from the 08:15 and 18:45 GMT profiles were not effected by this problem.

Figure 11a shows the July 17 lidar AEC profiles at 10:15 and 18:45 GMT. Figure 11a also shows the average AEC measured by the IZO nephelometer at both mid-day (Daytime) and after 18:00 GMT. The lidar AEC values at 2.442 km agree well with the IZO nephelometer AEC values. Figure 11b shows the lidar AOD profile at 18:45 GMT, the AATS-14 (onboard the Pelican aircraft) AOD profile from 18:30 to 18:45 GMT, and the AOD measured by the Teide shadowband and the IZO cimel for this time period. The AATS-14 AOD values immediately above the IZO altitude, average  $0.218 \pm 0.05$  AOD units. This portion of the Pelican flight corresponds to horizontal flight tracks across the mountain ridge, approximately 50 meters over IZO. The spread in AOD ( $\pm 0.05$ ) for these tracks is evidence of slight changes in the horizontal homogeneity of the dust layer overhead. The AOD values from all the instruments agree within approximately 0.02 AOD units for most of the profile and they agree better than the  $\pm 0.05$  AOD spread from horizontal inhomogeneity for the entire profile. The excellent agreement between the lidar 18:45 GMT data and the data from the other instruments for this time shows that the MPL calibrations and inversion algorithm worked successfully and that the BER calculated for this profile was accurate for this dust episode.

### **Dust Aerosol Backscatter-Extinction Ratios**

The calculated lidar BER values for the 08:15, 10:15, 17:15, and 18:45 GMT profiles were 0.026, 0.048, 0.073, and  $0.027 \text{ sr}^{-1}$  respectively. The same diurnal increase in the BER, as was present for the upslope aerosols, may exist during the dust episode because slightly higher BER values (average  $\sim 0.06 \text{ sr}^{-1}$ ) during mid-day relative to BER values for morning and late afternoon (average  $\sim 0.025 \text{ sr}^{-1}$ ) were calculated on July 17. However, the mid-day BER values may be inaccurate due to the calibration noise problem. Elevated BER values during mid-day could also be caused by the presence of a small

amount of small spherical upslope aerosols. However, analysis of this possible effect is beyond the scope of this paper.

Thus, attention was focused on the morning and late afternoon lidar profiles (08:15 and 18:45 GMT respectively) because they were not influenced by significant noise problems. The lidar  $P_A(\theta)$  value for these periods is approximately  $0.3 \text{ sr}^{-1}$ . Mie phase functions were calculated (O. Dubovik, personal communication) using the cimel data on July 17. The Mie phase function values at  $0^\circ$  were near  $200 \text{ sr}^{-1}$  at 08:00 GMT and near  $300 \text{ sr}^{-1}$  at 18:30 GMT. The Mie phase function values at  $180^\circ$  for 08:00 and 18:45 GMT were nearly identical and averaged approximately  $0.6 \text{ sr}^{-1}$ . The ratio of the lidar  $P_A(\theta)$  value with the Mie  $P_A(\theta)$  value from the cimel is  $\sim 0.5$  assuming  $g_o = 1$ , and the ratio is  $\sim 0.625$  assuming  $g_o = 0.8$ . The ratio of lidar to Mie  $P_A(\theta)$  values, calculated using ranges of  $g_o$  similar to those determined during this dust episode (Formenti et al., this issue; Schmid et al., this issue), agree well with the results presented in Mishchenko et al. (1997) for non-spherical particles. Therefore, the aerosols present during this dust episode were non-spherical. Also, comparison of the measured cimel and lidar phase function values with the phase functions in Plate 5 of Mishchenko et al. (1997) gives  $x_{\text{eff}}$  ranges from 16 to 20, corresponding to  $r_{\text{eff}}$  ranges from 1.3 to 1.7 microns (assuming the index of refraction  $1.53+0.008i$ ).

### **Dust Horizontal Lidar Signal Results**

Horizontal profiles (lidar aimed approximately due East) of the natural logarithm of the ABS on July 17 at 11:15 and 18:50 GMT are shown in Figure 12, along with a calculated Rayleigh profile for comparison. Both measured lidar profiles are non-linear within 2 km of IZO, indicating that horizontal homogeneity did not exist near the mountain ridge. The 11:15 GMT profile shows an increasing and non-linear plot out to about 1.5 km

in range, followed by a fairly linear (but noisy) plot from 1.5 to 4 km. The 18:50 GMT profile also shows a non-linear plot out to about 2.5 km, followed by a linear plot from 2.5 to 4 km. Therefore, the atmosphere does appear to be horizontally homogeneous from approximately 2 km to 4 km (the maximum horizontal range with dust present) away from the mountain ridge during this dust episode.

Both horizontal profiles show that the aerosols are not horizontally homogeneous close to the side of the ridge (out to about 2 km). However, the sharply increasing plot within the first kilometer of range for the 11:15 GMT profile shows that a large amount of aerosol was present within 1 km from the ridge relative to the situation at 18:50 GMT. The increase in aerosol within 1 km of the ridge during daytime (11:15 GMT) corresponds to the upslope period. The 18:50 GMT profile shows that less aerosol was located close to the mountain side (within 1 km), and corresponds to the period after the upslope has subsided (~18:00 GMT). The upslope wind motion may have changed the dust layer near the mountain and indicates the importance of considering upslope effects on the horizontal homogeneity of the region around IZO.

## **5. Conclusions**

The operation of the MPL system during ACE-2 has shown that this new lidar technology can be used successfully in the field. ACE-2 closure comparisons between the MPL system and other independently operated instruments have shown that the MPL calibration procedures and inversion algorithm succeed in producing accurate optical profiles throughout the entire range of the profile. This is significant because it shows that the overlap and afterpulse problems can be overcome, even when the MPL has suffered an instrument problem.

The results of lidar analysis during ACE-2 have shown several interesting characteristics of the upslope aerosols and the Saharan dust episode during the middle of

the experiment. The upslope aerosols were seen to form a layer several hundred meters above and to the sides of IZO during the day, and to subside by nightfall. The peak AEC values obtained in these upslope aerosol layers were low compared to MBL values, but were approximately 25% greater than Rayleigh values. The dust layer on July 17 was seen to reside mostly above and to the sides of IZO, possibly held off by the motion of upslope winds despite findings that show upslope winds have been known to be weaker during dust episodes (Raes et al., 1997). The possible perturbation of the dust layer by the upslope effect is significant due to the fact that the IZO site is used during summer months to study Saharan dust layers. Peak AEC values obtained during the dust episode were an order of magnitude higher than Rayleigh values. Finally, the dust layer altitude ranges observed during ACE-2 (from just over 2 km to under 5 km) correspond well with other investigations of the vertical structure of the Saharan air layer (SAL) over the North Atlantic Ocean (Carlson and Prospero, 1972; Karyampudi and Carlson, 1988).

Results of this study also show that upslope aerosols ( $r_{\text{eff}}$  from 0.5 to 0.8 microns) are smaller relative to aerosols during the dust episode ( $r_{\text{eff}}$  from 1.3 to 1.7 microns). The differences in  $r_{\text{eff}}$  values between upslope and dust conditions agree well Angstrom exponents measured with the IZO cimel during ACE-2 (Smirnov et al., 1998). The Angstrom exponent during upslope conditions on June 29 was approximately 1.0, indicating may small particles, and the Angstrom exponent during the afternoon of the July 17 dust episode averaged 0.16, indicating a greater portion of larger particles. Another important result was the determination of an accurate BER value ( $0.025 \text{ sr}^{-1}$ ) for the dust episode on July 17. Knowledge of an accurate BER during dust episodes will aid in the analysis of future lidar measurements in regions influenced by dust aerosols. Finally, the degree of non-sphericity of the upslope aerosols was found to be small, but the degree of non-sphericity of the aerosols during the dust episode was large and found to be in agreement with previous theoretical studies of dust-like aerosols.

Several areas requiring further study have also been identified. Using the initial results from work presented in this study and others in this issue, more in-depth comparisons and analysis of data from the different measurement platforms will be addressed in future work. In addition to more accurate results of the type discussed in this study, attention will be given to correct determination of the altitude dependence of the index of refraction and the single scattering albedo. This will in turn produce better lidar inversions and help to determine the correct BER for both the upslope and dust aerosols. Lastly, further studies of the horizontal homogeneity of the region surrounding IZO will be attempted.

## **Appendix: The Lidar Inversion Algorithm**

The lidar inversion algorithm used for this study is presented in this section. Also, errors inherent to the algorithm are discussed. The primary error is due to the assumption of a constant BER value,  $R_A$ .

### **The Solution to the Lidar Equation**

The basic  $S_A(z)$  solution to lidar data taken according to Eq. (3) is referred to as the backward Fernald two-component solution (Fernald et al., 1972) as it uses the value of the backscattering coefficient at some maximum altitude,  $z_m$ , as a boundary value and then successive values of  $S_A(z)$  are calculated as the altitude is decreased toward the lidar altitude,  $z_L$ . The solution is given below in a format for algorithm development (Fernald, 1984),

$$S_A(x-1) = \frac{S_r(x-1) S_A(x-1, x)}{\frac{S_r(x)}{S_A(x) + S_R(x)} + \frac{1}{R_A} [S_r(x) + S_r(x-1) S_A(x-1, x)] z} - S_R(x-1), \quad (\text{A.1})$$

where



$$(x - 1, x) = \exp \left( \frac{1}{R_A} - \frac{1}{R_R} \right) \left( R_R(x - 1) + R_R(x) \right) z, \quad (A.1)$$

and  $x$  is the altitude bin one step above  $x-1$ , and  $z$  is the lidar range interval (75 m). In order to obtain the extinction coefficient profile, each value of the backscattering coefficient need only be divided by  $R_A$ .

The basic lidar algorithm that uses Eq. (A.1) to solve for the aerosol profiles must assume that  $R_A$  and the backscattering coefficient at some maximum altitude,  $\beta_A(z_m)$ , are known.  $R_A$  is not usually known, but the latter constraint is usually valid as aerosols are normally confined to the marine boundary layer (MBL), or at least at low altitudes above the lidar (such as over IZO), therefore,  $z_m$  can be chosen at an altitude where  $\beta_A(z_m) = 0$ . An algorithm was developed for this study that uses an independently measured AOD,  $A_{\lambda}$ , as input and produces a  $\beta_A$  profile that integrates to the measured AOD and will also calculate the value of  $R_A$ .

### The Lidar Inversion Algorithm

This algorithm is based on procedures described in Fernald et al. (1972) and Marenco et al. (1997). The algorithm produces extinction coefficient and AOD profiles, and also calculates the BER. The algorithm is described below and presented schematically in Figure 13.

The first step in the algorithm requires determination of  $\beta_A$  at some maximum altitude,  $z_m$ , and is done by inspection of the calibrated signals. Inspection of the signals during ACE-2 showed that there was a maximum altitude, above which, no aerosol appeared to be present ( $\beta_A \sim 0$ ). The inversion algorithm value of  $z_m$  was chosen to lie just above this altitude, with  $\beta_A$  set equal to 0.

The second step in the algorithm is the calculation of  $\beta_A$  one altitude step, 75 m, below  $z_m$ . This is done by solving Eq. (A.1) with  $\beta_A(x=z_m) = 0$ , and the Rayleigh profile quantities;  $\beta_R(z)$ ,  $\beta_R(z)$ , and  $R_R$ , from Hansen and Travis (1974). In order to solve Eq. (A.1),  $R_A$  is required. For this step in the algorithm,  $R_A$  is set equal to 1 and  $\beta_A(x-1)$  is calculated. This process is repeated downward through the atmosphere, with  $R_A = 1$  and  $\beta_A(x+1)$  obtained from the previous step, until the value of  $\beta_A$  is calculated at the lowest altitude bin (75 m above the MPL system altitude).

The next step in the algorithm is to improve the estimate of  $R_A$  (determination of  $R_{A \text{ new}}$ ). The new value for  $R_A$  is determined using the backscattering coefficient profile calculated in the previous step (with  $R_A = 1$ ) and the independently measured AOD,  $A$ .  $R_{A \text{ new}}$  is calculated using the following equation,

$$R_{A \text{ new}} = \frac{\int_{z_L}^{z_m} \beta_A(z) dz}{A} \quad (\text{A.2})$$

with  $A$  from the independent measurement. The backscattering coefficient profile is now recalculated, using  $\beta_A(x=z_m) = 0$ , but with  $R_A = R_{A \text{ new}}$ . This step is continued until successive values of  $R_A$  and  $R_{A \text{ new}}$  differ negligibly (percent difference between  $R_A$  and  $R_{A \text{ new}}$  less than 0.5). The final backscattering coefficient profile and  $R_A$  are then used to calculate the extinction coefficient profile,  $\beta_A(z)$ . The extinction coefficient profile is then numerically integrated from  $z_L$  to  $z_m$ , and then subtracted from  $A$  at each altitude step, to produce an AOD profile,  $\beta_A(z)$ . Thus the final data products from the algorithm are the extinction coefficient and AOD profiles and  $R_A$ .

### **Errors in the Results from the Lidar Inversion Algorithm**

This algorithm was tested with artificial lidar data to study the effects of errors caused by the algorithm and the assumption of a constant  $R_A$  (Welton, 1998). Both a single and a two aerosol species atmosphere were tested. The results show that in a single aerosol species atmosphere (with constant  $R_A$ ) the algorithm accurately calculates the  $\sigma_A(z)$  profile and the correct  $R_A$  (and thus accurate  $\sigma_A(z)$  and AOD profiles) even if the concentration of the aerosols varies vertically and the aerosols are separated into different layers. For cases with two aerosol species with different  $R_A$  values and different backscattering coefficient profiles, the results show that the algorithm was found to calculate an  $R_A$  value that was an accurate average of the two different true  $R_A$  values whether the species were in one continuous layer (but not mixed together) or separated into two distinct layers. For real situations, different aerosol species are often mixed together and it is expected that the final BER calculated will be dependent more on the relative amounts of each aerosol and will not produce a direct average of the different individual BER values. However, the algorithm will produce an accurate columnar value of the  $R_A$  in real situations. This is an important result since other ground-based instruments that also measure  $R_A$  related quantities, such as the aerosol phase function, also produce columnar values because they measure the entire atmospheric column.

Errors were present in the resulting  $\sigma_A(z)$  profiles when the constant  $R_A$  inversion algorithm was applied to an inhomogeneous  $R_A$  atmosphere. The initial  $\sigma_A(z)$  profile values near  $z_m$  are correct but successive values of  $\sigma_A$  deviate from the correct value, this and the calculation of an average  $R_A$  then effect the calculation of the  $\sigma_A(z)$  profile. The algorithm forces the final  $\sigma_A(z)$  profile to integrate to the correct  $R_A$  value. The value,  $\sigma_A/R_A$  will be

iterated continually, until the correct  $R_A$  value is reached. If the  $R_A$  value used is incorrect, then the resulting  $R_A$  profile will have errors.

These types of  $R_A$  related errors have been studied by other researchers in depth (Klett, 1985; Sasano et al., 1985; Kovalev, 1993; Kovalev and Moosmuller, 1994). In order to attempt to overcome errors associated with the choice of a constant  $R_A$ , these researchers have constructed algorithms using range dependent  $R_A$  values. However, for these algorithms an  $R_A$  profile, from model or data, must be used. The choice was made to use a constant  $R_A$  algorithm for this study since neither data, nor models of  $R_A$ , were available during the lidar campaigns.

## **Acknowledgments**

This research is a contribution to the International Global Atmospheric Chemistry (IGAC) core project of the International Geosphere-Biosphere Programme (IGBP) and is part of the IGAC Aerosol Characterization Experiments (ACE). The authors extend great appreciation to E. Cuevas, R. Juega Buide, and the rest of the Izaña observatory staff for their support during ACE-2. Thanks is also given to O. Dubovik for providing the cimel phase functions, and to A. Chapin for invaluable work in preparing the micro-pulse lidar system for field use. Funding for the measurements and analyses presented in this work was provided by the National Aeronautics and Space Administration, US National Science Foundation, Office of Naval Research, European Commission DG XII (Environment and Climate), Max Planck Society, and the National Oceanic and Atmospheric Administration.

## **References**

Carlson, T.N., and Prospero, J.M. 1972. The large-scale movement of Saharan air outbreaks over the Northern Equatorial Atlantic. *J. Appl. Meteorol.* **11**, 283-297.

Fernald, F.G., Herman, B.M., and Reagan, J.A. 1972. Determination of aerosol height distributions by lidar. *J. Appl. Meteorol.* **11**, 482-489.

Fernald, F.G. 1984. Analysis of atmospheric lidar observations: some comments. *Appl. Optics* **23**, 652-653.

Formenti, P., Andreae, M.O., and Lelieveld, J. 1998. Saharan Dust Occurrence at a mid-tropospheric site in Tenerife. *J. Aerosol Sci.* **29**, S1047-S1048.

Formenti, P., Andreae, M.O., and Lelieveld, J. 1999. Measurements of aerosol optical depth in the North Atlantic free troposphere: results from ACE-2. *Tellus*, submitted this issue.

Heintzenberg, J., and Russell, P.B. 1999. An Overview of the ACE 2 Clear Sky Column Closure Experiment (CLEARCOLUMN). *Tellus*, submitted this issue.

Hansen, J.E., and Travis, L.D. 1974. Light scattering in planetary atmospheres. *Space Sci. Reviews* **16**, 527-610.

Holben, B.N., Eck, T.F., Slutsker, I., Tanre, D., Buis, J.P., Setzer, A., Vermote, E., Reagan, J.A., Kaufman, Y.J., Nakajima, T., Lavenue, F., Jankowiak, I., and Smirnov, A. 1998. AERONET-A federated instrument network and data archive for aerosol characterization. *Rem. Sens. Environ.* **66**, 1-16.

- Karyampudi, V.M., and Carlson, T.N. 1988. Analysis and numerical simulations of the Saharan Air Layer and its effects on easterly wave disturbances. *J. Atmos. Sci.* **45**, 3102-3136.
- Klett, J.D. 1985. Lidar inversion with variable backscatter/extinction ratios. *Appl. Optics* **24**, 1638-1643.
- Kovalev, V.A. 1993. Lidar measurement of the vertical aerosol extinction profiles with range-dependent backscatter-to-extinction ratios. *Appl. Optics* **32**, 6053-6065.
- Kovalev, V.A., and Moosmuller, H. 1994. Distortion of particulate extinction profiles measured with lidar in a two-component atmosphere. *Appl. Optics* **33**, 6499-6507.
- Marenco, F., Santacesaria, V., Bais, A.F., Balis, D., di Sarra, A., Papayannis, A., and Zerefos, C. 1997. Optical properties of tropospheric aerosols determined by lidar and spectrophotometric measurements (Photochemical Activity and Solar Ultraviolet Radiation campaign). *Appl. Optics* **36**, 6875-6886.
- Mishchenko, M.I., Travis, L.D., Kahn, R.A., and West, R.A. 1997. Modeling phase functions for dustlike tropospheric aerosols using a shape mixture of randomly oriented polydisperse spheroids. *J. Geophys. Res.* **102**, 16831-16847.
- Prospero, J.M., Schmitt, R., Cuevas, E., Savoie, D., Graustein, W., Turekian, K., Volz-Thomas, A., Oltmans, S., Levy, H., and Diaz, A. 1995. Temporal variability of ozone and aerosols in the free troposphere over the Eastern North Atlantic. *Geophys. Res. Letts.* **22**, 2925-2928.

Raes, F., Van Dingenen, R., Cuevas, E., Van Velthoven, P.F.J., and Prospero, J.M. 1997. Observations of aerosols in the free troposphere and marine boundary layer of the subtropical Northeast Atlantic: Discussion of processes determining their size distribution. *J. Geophys. Res.* **102**, 21315-21328.

Raes, F., Bates, T., Verver, G., Vogelenzang, D., and Van Liedekerke, M. 1999. The Second Aerosol Characterization Experiment (ACE-2): introduction, meteorological overview and main results. *Tellus*, submitted this issue.

Sasano, Y., Browell, E.V., and Ismail, S. 1985. Error caused by using a constant extinction/backscattering ratio in the lidar solution. *Appl. Optics* **24**, 3929-3932.

Schmid, B., Livingston, J.M., Russell, P.B., Durkee, P.A., Jonsson, H.H., Collins, D.R., Flagan, R.C., Seinfeld, J.H., Gassó, S., Hegg, D.A., Öström, E., Noone, K.J., Welton, E.J., Voss, K.J., Gordon, H.R., Formenti, P., and Andreae, M.O. 1999. Clear sky closure studies of lower tropospheric aerosol and water vapor during ACE-2 using airborne sunphotometer, airborne in-situ, space-borne, and ground-based measurements. *Tellus*, submitted this issue.

Smirnov, A., Holben, B.N., Slutsker, I., Welton, E.J., and Formenti, P. 1998. Optical Properties of Saharan Dust During ACE 2. *J. Geophys. Res.* **103**, 28079-28092.

Spinhirne, J.D. 1993. Micro pulse lidar. *IEEE Trans. Geosci. Remote Sens.* **31**, 48-55.

Spinhirne, J.D., Rall, J., and Scott, V.S. 1995. Compact eye-safe lidar systems. *Rev. Laser Eng.* **23**, 26-32.

Welton, E.J. 1998. Measurements of Aerosol Optical Properties over the Ocean Using Sunphotometry and Lidar. *Ph.D. Dissertation*. University of Miami, Coral Gables, 1-150.

## **List of Figure Captions**

Figure 1. Schematic diagram of the micro-pulse lidar system (not to scale).

Figure 2a. Aerosol total mass concentrations ( $\mu\text{g m}^{-3}$ ) measured during the early mornings of June 29 and July 15 1997 at IZO.

Figure 2b. Aerosol extinction coefficients ( $\text{m}^{-1}$ ) measured during the early mornings of June 29 and July 15 1997 at IZO.

Figure 3a. Overlap functions,  $O(z)$ , calculated on June 29 and July 15 1997.

Figure 3b. Afterpulse functions,  $A(z)$ , calculated on June 29 and July 15 1997.

Figure 4. The measured MPL signal, a calculated Rayleigh lidar signal, and the final calibrated MPL signal are shown for 00:00 GMT on June 30, 1997.

Figure 5. Three-day attenuated backscatter signal (ABS) ( $\text{m sr}^{-1}$ ) time series from June 29 through July 1, 1997. Each major tickmark separates the days, and each minor tickmark is one hour (GMT).

Figure 6a. Attenuated Backscatter Signals ( $\text{m sr}^{-1}$ ) on June 29, 1997. Each profile is a 15 minute average, starting 15 minutes prior to the time shown. The 06:15 GMT (before



sunrise) profile shows no evidence of upslope aerosols and is representative of a clean, Rayleigh-only lidar profile. Upslope aerosols are visible up to approximately 5 km for the 07:15 GMT and 10:15 GMT profiles (during daytime).

Figure 6b. Attenuated Backscatter Signals ( $\text{m sr}^{-1}$ ) on June 29, 1997. Each profile is a 15 minute average, starting 15 minutes prior to the time shown. Upslope aerosols are visible up to approximately 5 km for the 17:15 GMT and 19:15 GMT profiles (during daytime). The 22:15 GMT (after sunset) profile shows no evidence of upslope aerosols and is representative of a clean, Rayleigh-only lidar profile.

Figure 7a. Lidar aerosol extinction coefficient ( $\text{m}^{-1}$ ) profiles at 08:15, 10:15, 17:15, and 18:15 GMT on June 29, 1997. The columnar AOD for each profile is 0.017, 0.018, 0.015, and 0.014 respectively. The calculated columnar backscatter-extinction ratios ( $\text{sr}^{-1}$ ) for each profile are 0.018, 0.038, 0.031, and 0.017 respectively. The Rayleigh extinction coefficient profile is shown for comparison. The average aerosol extinction coefficient measured by the IZO nephelometer from 07:00 to 19:00 GMT is also shown.

Figure 7b. Lidar aerosol optical depth (AOD) profiles at 08:15, 10:15, 17:15, and 18:15 GMT on June 29, 1997. The columnar AOD for each profile is 0.017, 0.018, 0.015, and 0.014 respectively. The calculated columnar backscatter-extinction ratios ( $\text{sr}^{-1}$ ) for each profile are 0.018, 0.038, 0.031, and 0.017 respectively. The average AOD measured by the Teide shadowband is also shown.

Figure 8. Horizontal lidar profiles of the natural logarithm of the attenuated backscatter coefficient ( $\text{m sr}^{-1}$ ). A 15 minute average horizontal profile at 10:45 GMT on June 29 is shown along with a calculated Rayleigh horizontal profile for the IZO altitude.

Figure 9. Three-day attenuated backscatter signal (ABS) ( $\text{m sr}^{-1}$ ) time series from July 16 through July 18, 1997. Each major tickmark separates the days, and each minor tickmark is one hour (GMT).

Figure 10. Lidar aerosol extinction coefficient ( $\text{m}^{-1}$ ) profiles at 08:15, 10:15, 17:15, and 18:45 GMT on July 17, 1997. The columnar AOD for each profile is 0.161, 0.205, 0.226, and 0.217 respectively. The calculated columnar backscatter-extinction ratios ( $\text{sr}^{-1}$ ) for each profile are 0.026, 0.048, 0.073, and 0.027 respectively. The Rayleigh extinction coefficient profile is shown for comparison.

Figure 11a. Lidar aerosol extinction coefficient ( $\text{m}^{-1}$ ) profiles at 10:15 and 18:45 GMT on July 17, 1997. The columnar AOD for each profile is 0.205 and 0.217 respectively. The calculated columnar backscatter-extinction ratios ( $\text{sr}^{-1}$ ) for each profile are 0.048 and 0.027 respectively. The average aerosol extinction coefficients measured by the IZO nephelometer from 07:00 to 18:00 GMT (daytime) and after 18:00 GMT are also shown.

Figure 11b. Lidar aerosol optical depth (AOD) profile at 18:45 GMT on July 17, 1997. The columnar AOD is 0.217 and the calculated columnar backscatter-extinction ratio ( $\text{sr}^{-1}$ ) is 0.027. The AOD profile measured with AATS-14 from 18:30 to 18:45 GMT, and the AOD measured by the IZO cimel and the Teide shadowband, are also shown.

Figure 12. Horizontal lidar profiles of the natural logarithm of the attenuated backscatter coefficient ( $\text{m sr}^{-1}$ ). A 15 minute average horizontal profile at 11:15 GMT and a 5 minute average horizontal profile at 18:50 GMT on July 17 are shown along with a calculated Rayleigh horizontal profile for the IZO altitude.

Figure 13. Schematic representation of the lidar inversion algorithm.

Figure 1

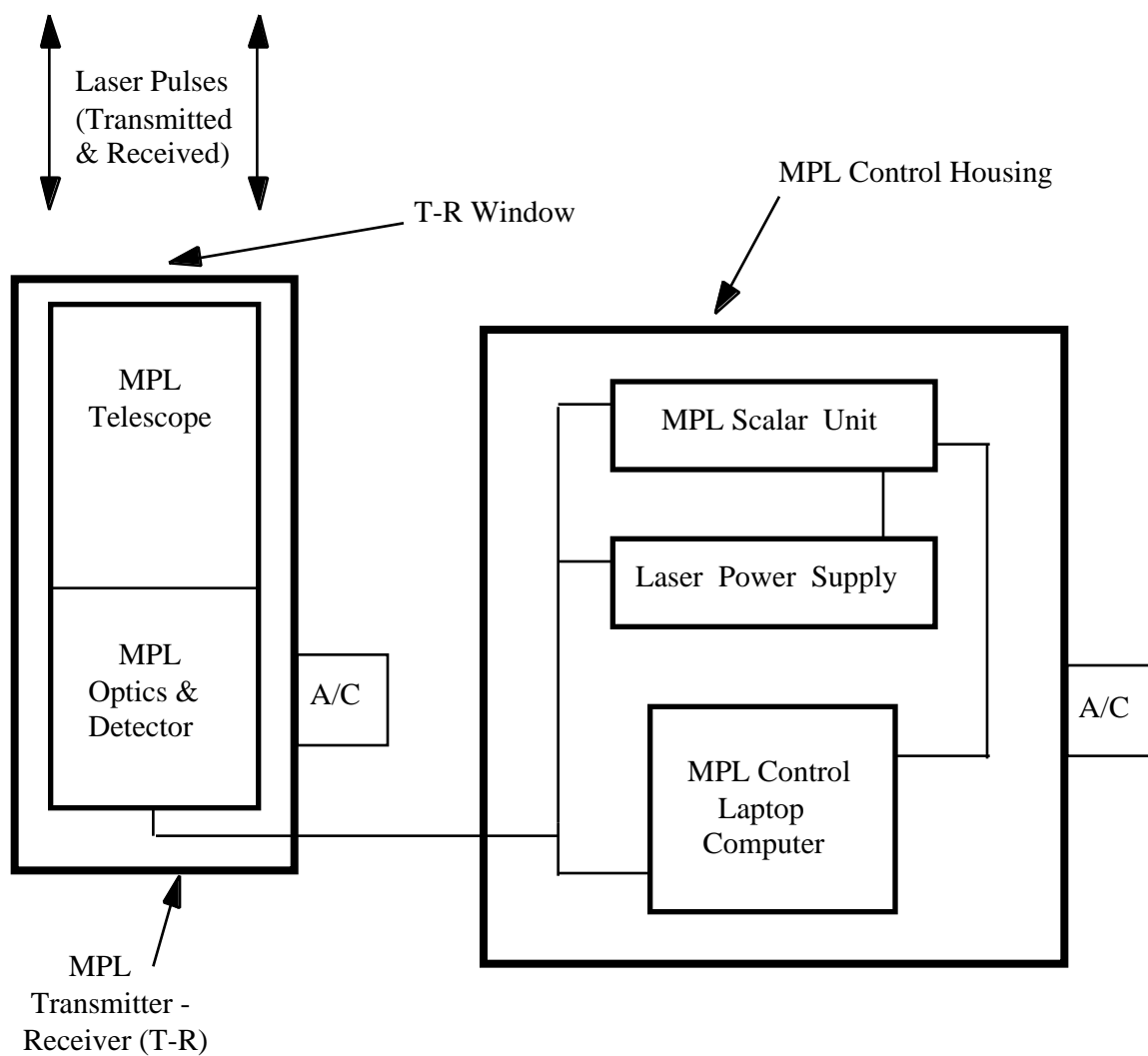


Figure 1. Schematic diagram of the micro-pulse lidar system (not to scale).

Figure 2a

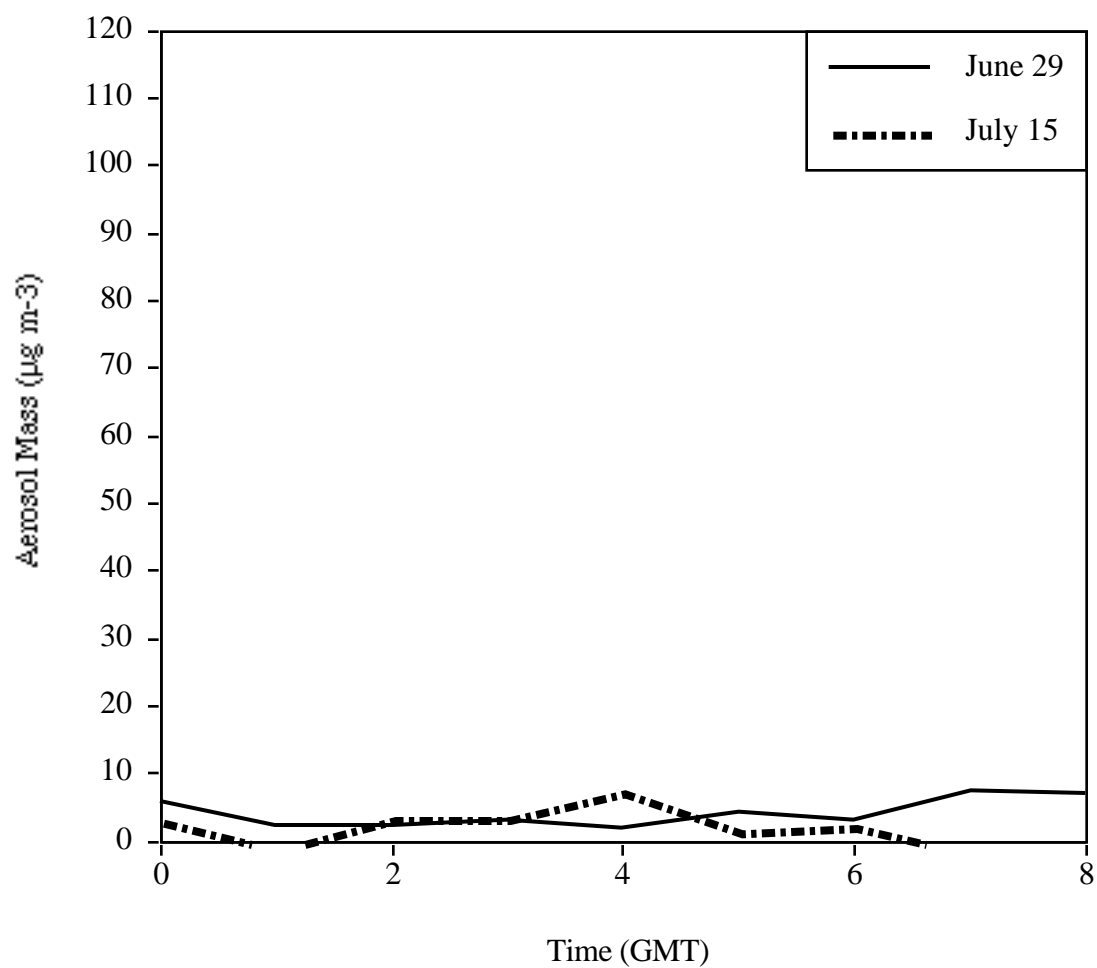


Figure 2a. Aerosol total mass concentrations measured during the early mornings of June 29 and July 15 1997 at IZO.

Figure 2b

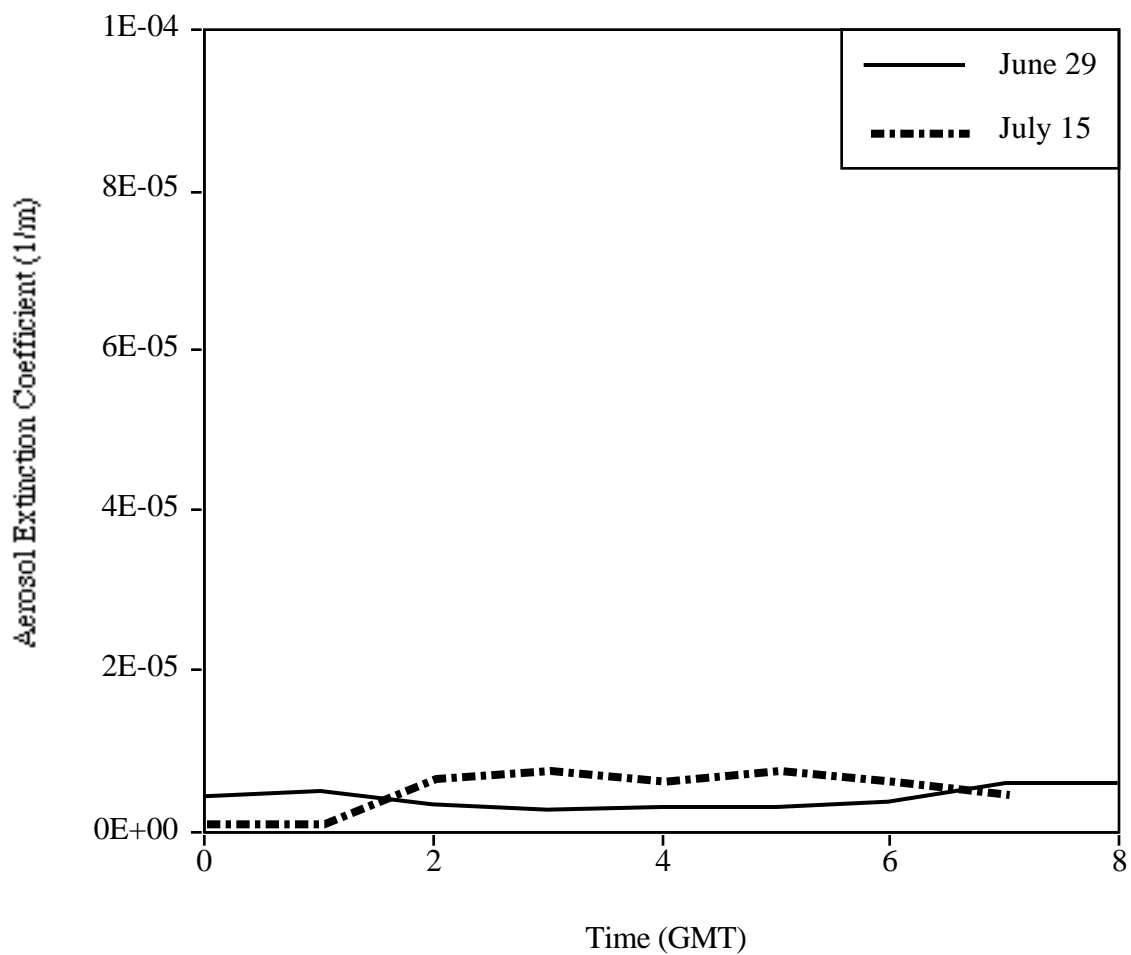


Figure 2b. Aerosol extinction coefficients measured during the early mornings of June 29 and July 15 1997 at IZO.

Figure 3a

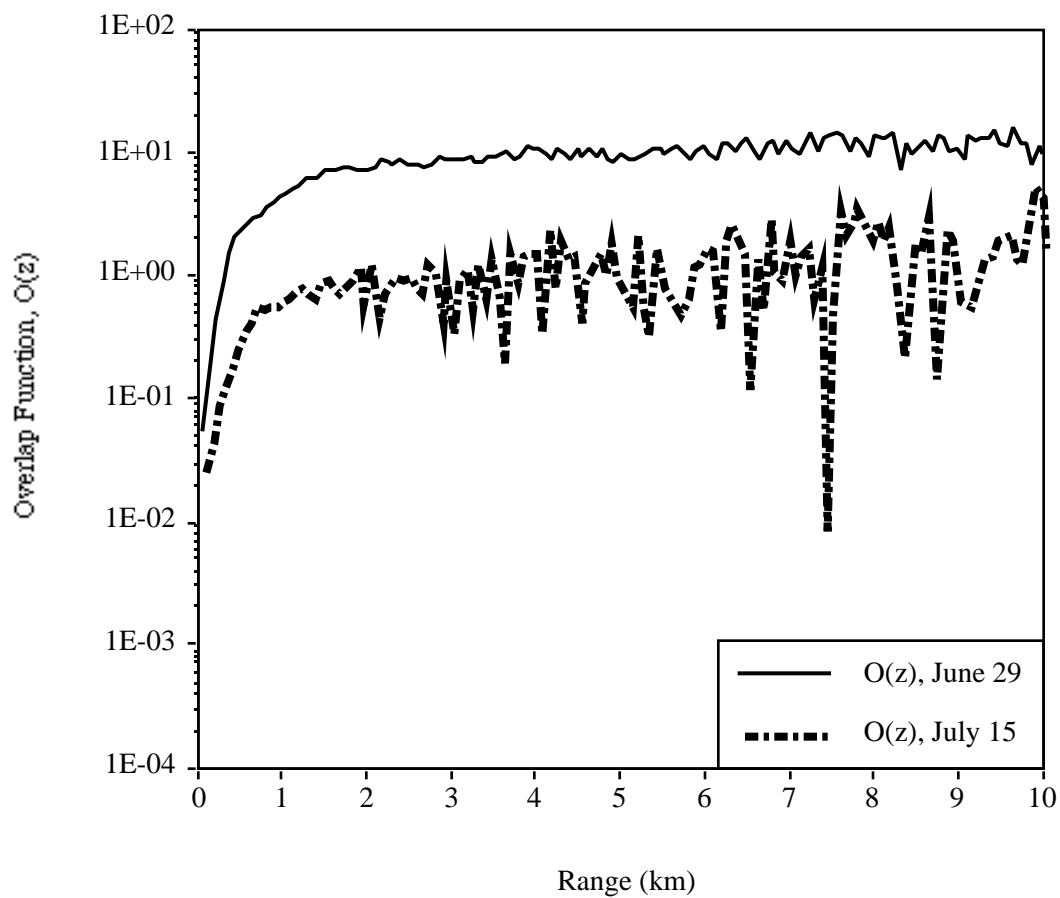


Figure 3a. Overlap functions,  $O(z)$ , calculated on June 29 and July 15 1997.

Figure 3b

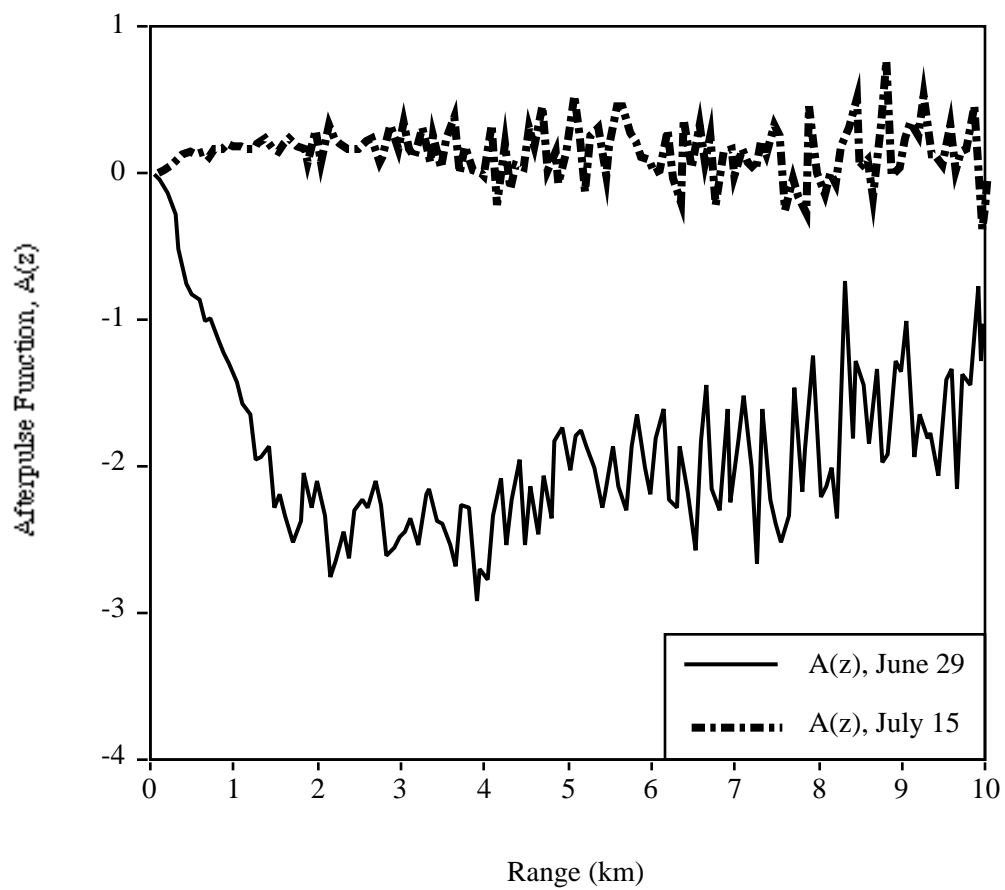


Figure 3b. Afterpulse functions,  $A(z)$ , calculated on June 29 and July 15 1997.



Figure 4

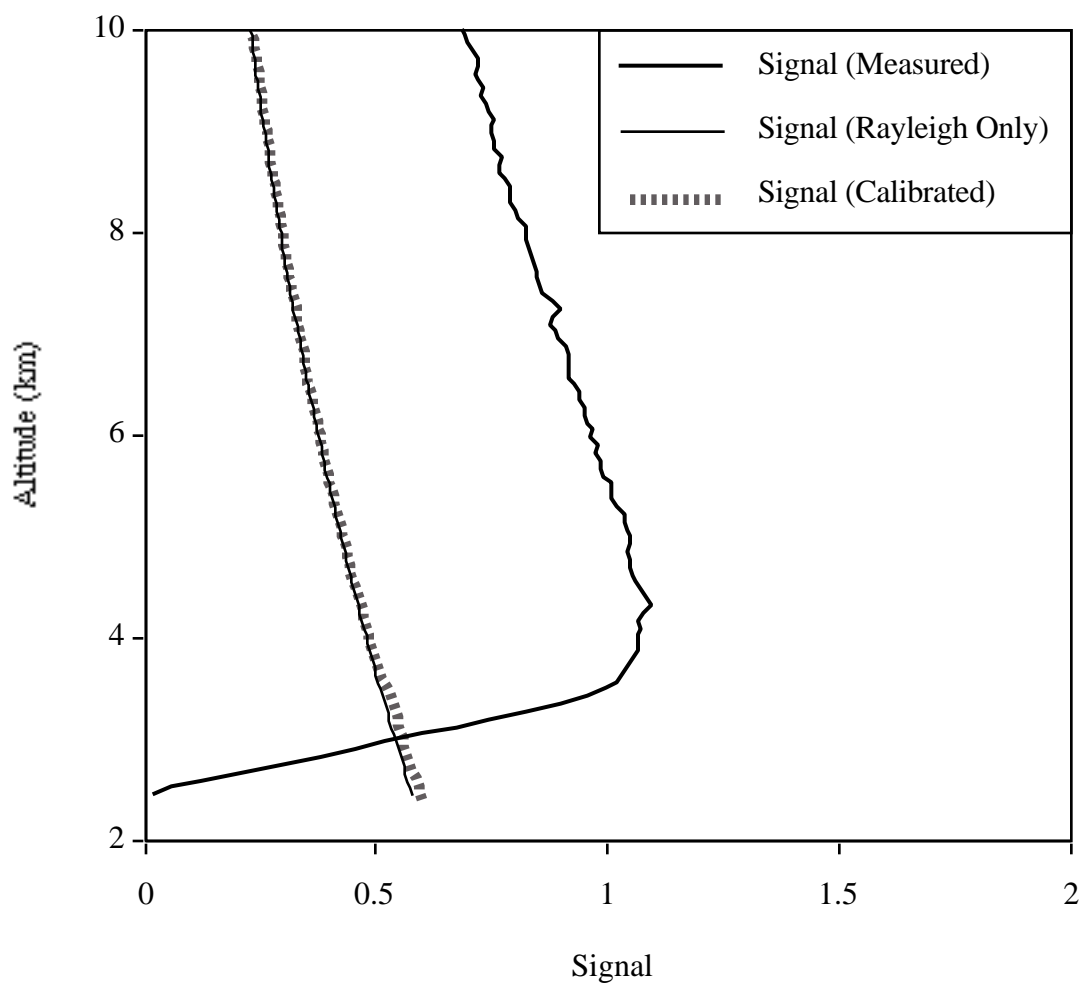


Figure 4. The measured MPL signal, a calculated Rayleigh lidar signal, and the final calibrated MPL signal are shown for 00:00 GMT on June 30, 1997.

Figure 5

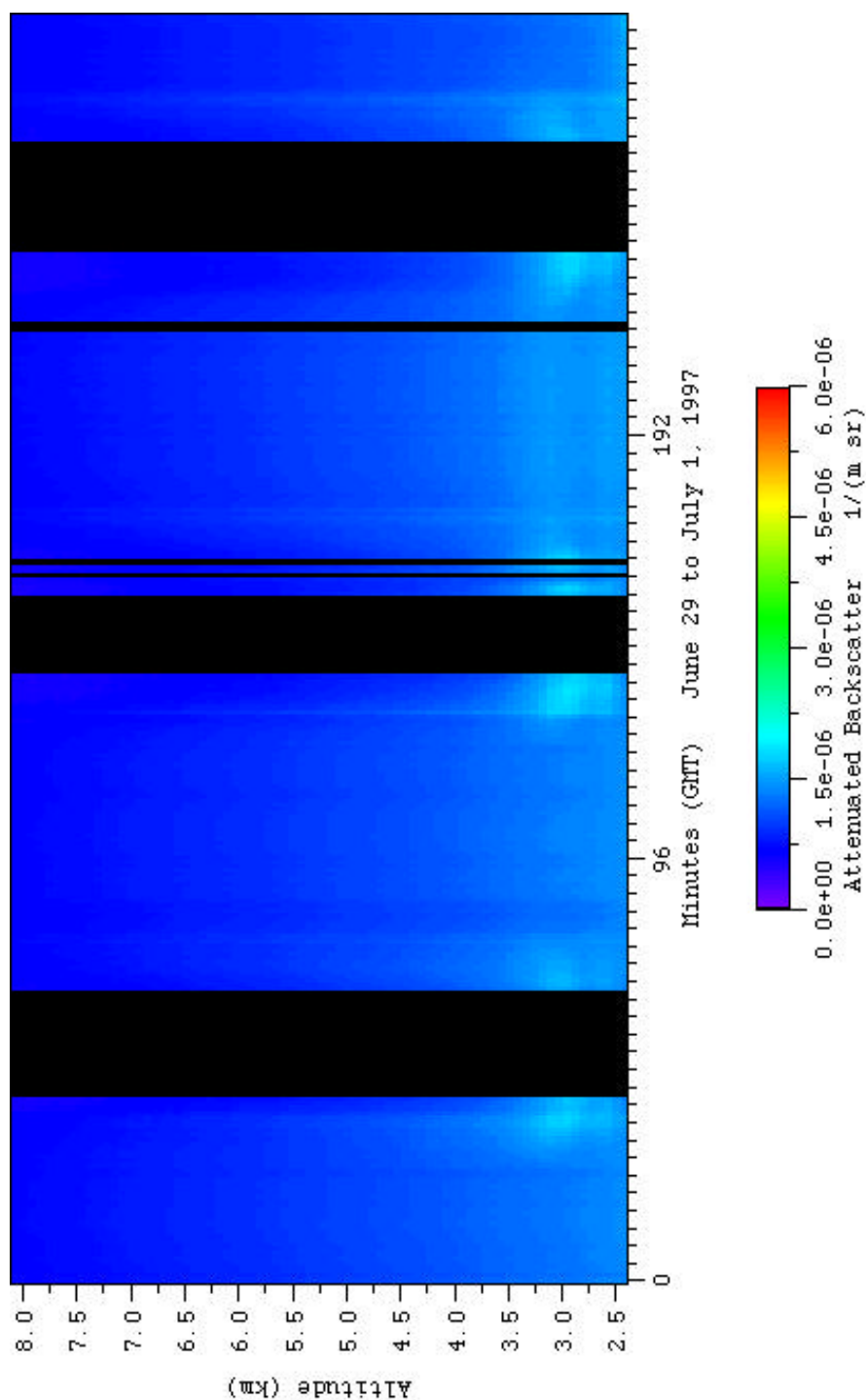


Figure 5. Three-day attenuated backscatter signal (ABS)  $(\text{m sr})^{-1}$  time series from June 29 through July 1, 1997. Each major tickmark separates the days, and each minor tickmark is one hour (GMT).

Figure 6a

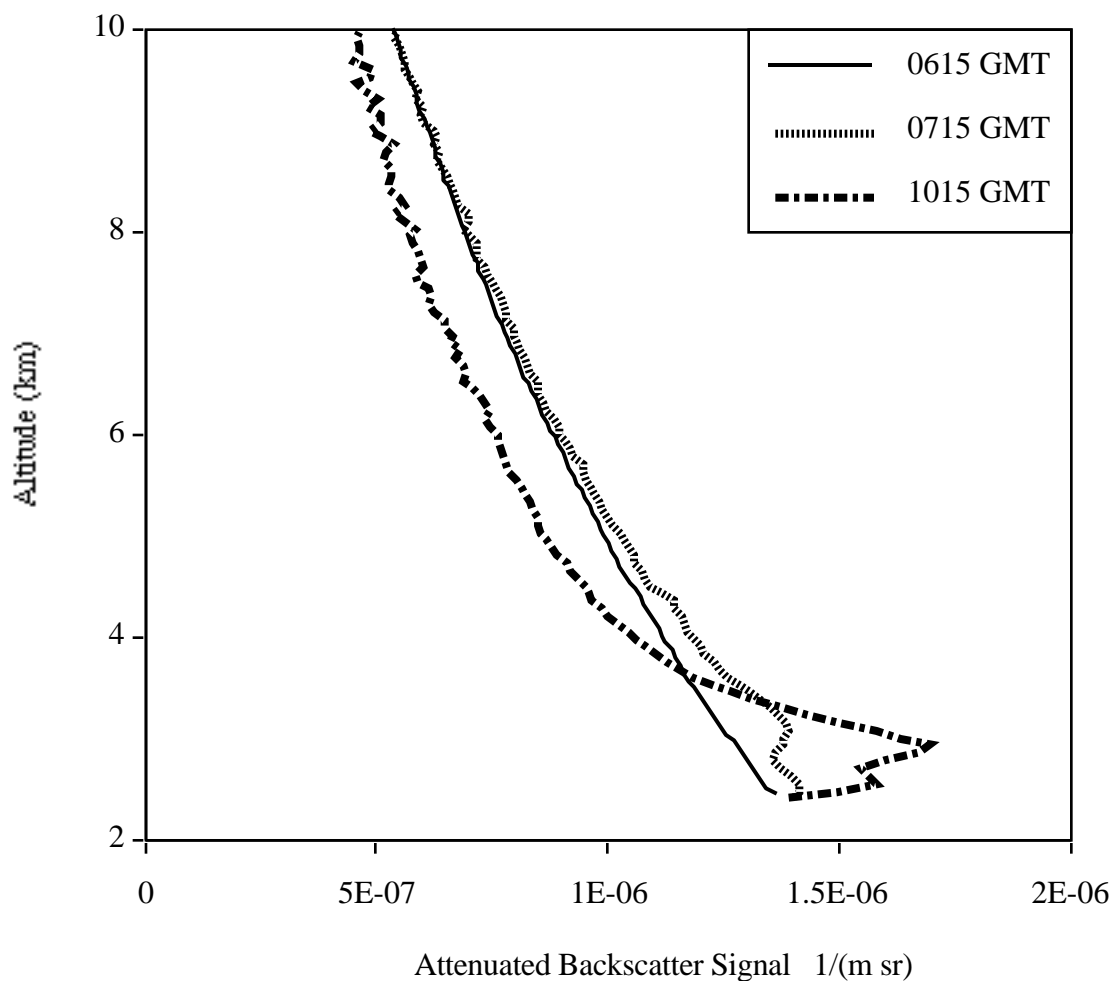


Figure 6a. Attenuated Backscatter Signals,  $1/(\text{m sr})$ , on June 29, 1997. Each profile is a 15 minute average, starting 15 minutes prior to the time shown. The 06:15 GMT (before sunrise) profile shows no evidence of upslope aerosols and is representative of a clean, Rayleigh-only lidar profile. Upslope aerosols are visible up to approximately 5 km for the 07:15 GMT and 10:15 GMT profiles (during daytime).

Figure 6b

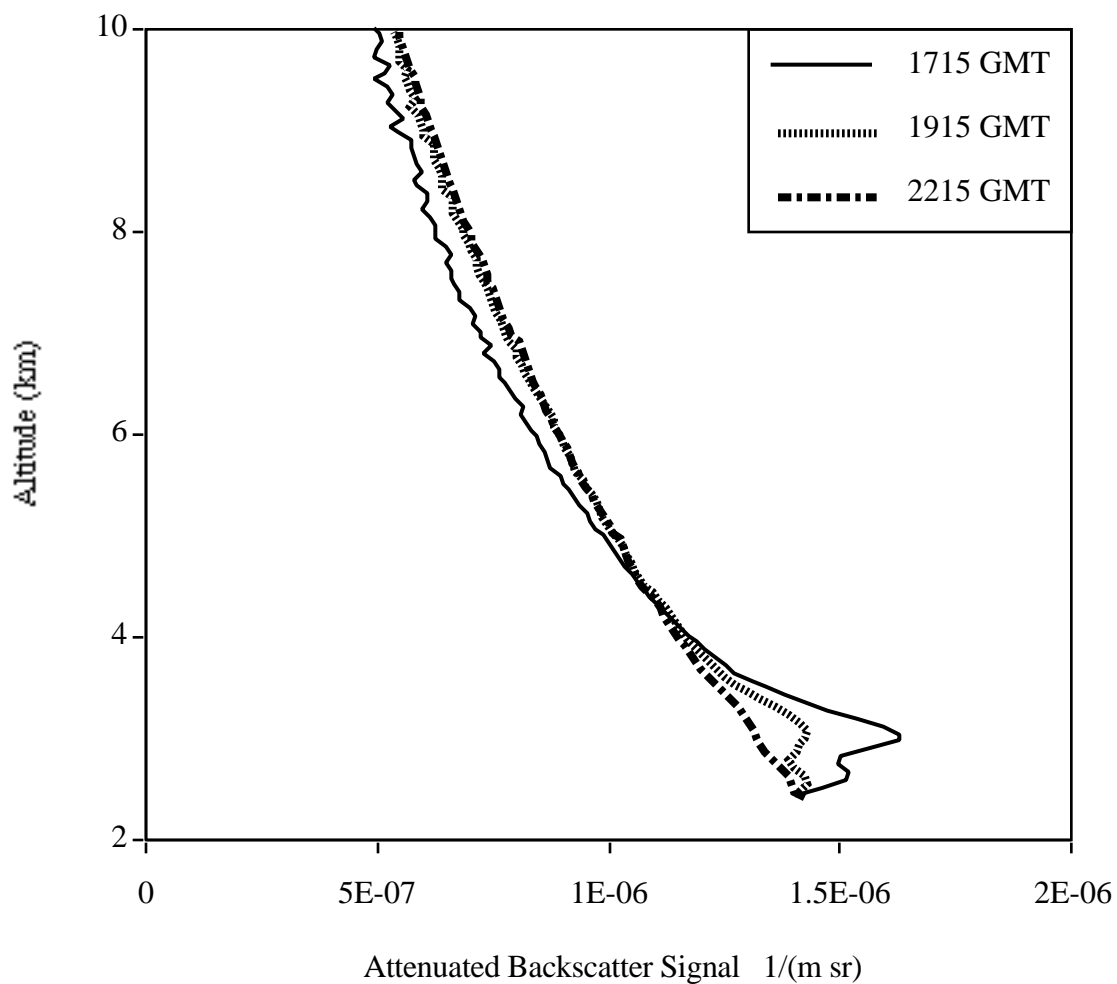


Figure 6b. Attenuated Backscatter Signals,  $1/(\text{m sr})$ , on June 29, 1997. Each profile is a 15 minute average, starting 15 minutes prior to the time shown. Upslope aerosols are visible up to approximately 5 km for the 17:15 GMT and 19:15 GMT profiles (during daytime). The 22:15 GMT (after sunset) profile shows no evidence of upslope aerosols and is representative of a clean, Rayleigh-only lidar profile.

Figure 7a

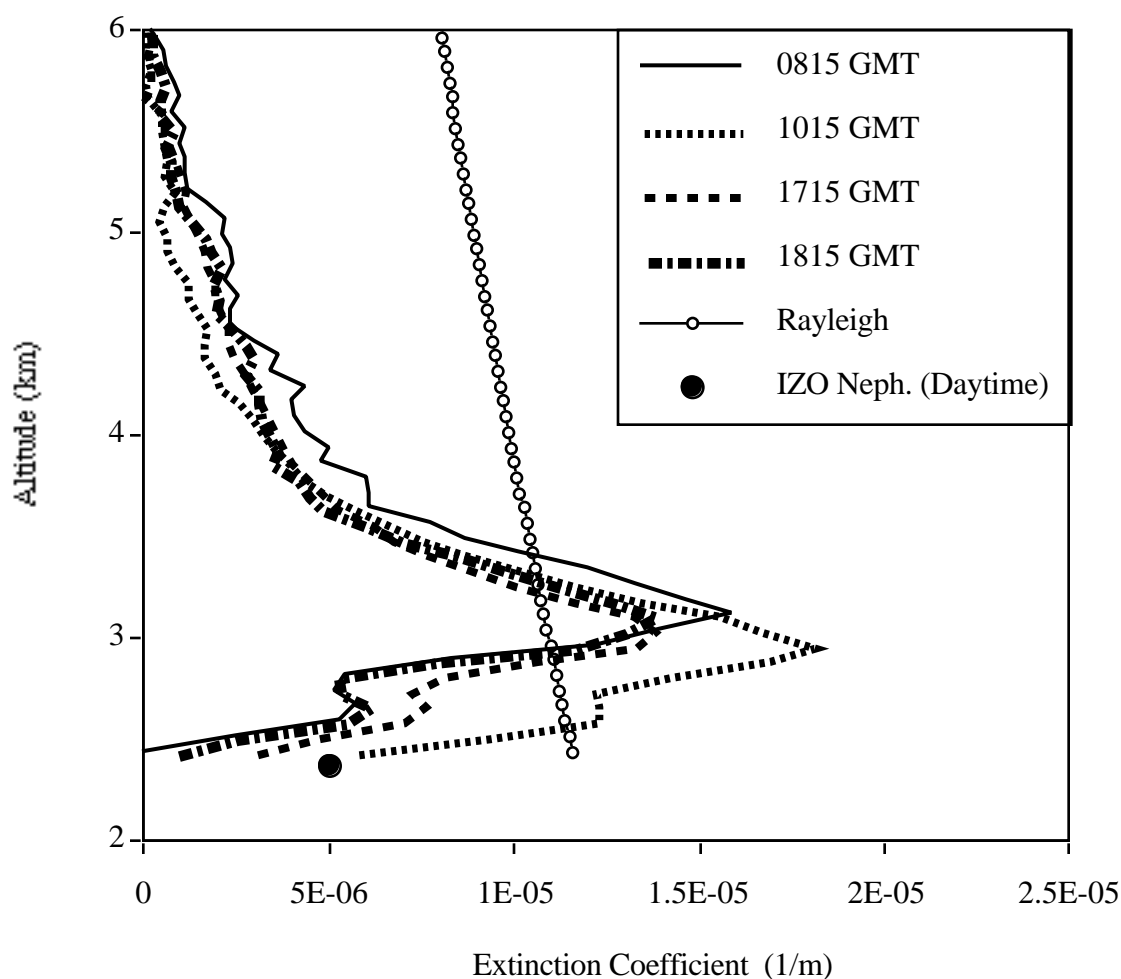


Figure 7a. Lidar aerosol extinction coefficient (1/m) profiles at 08:15, 10:15, 17:15, and 18:15 GMT on June 29, 1997. The columnar AOD for each profile is 0.017, 0.018, 0.015, and 0.014 respectively. The calculated columnar backscatter-extinction ratios (1/sr) for each profile are 0.018, 0.038, 0.031, and 0.017 respectively. The Rayleigh extinction coefficient profile is shown for comparison. The average aerosol extinction coefficient measured by the IZO nephelometer from 07:00 to 19:00 GMT is also shown.

Figure 7b

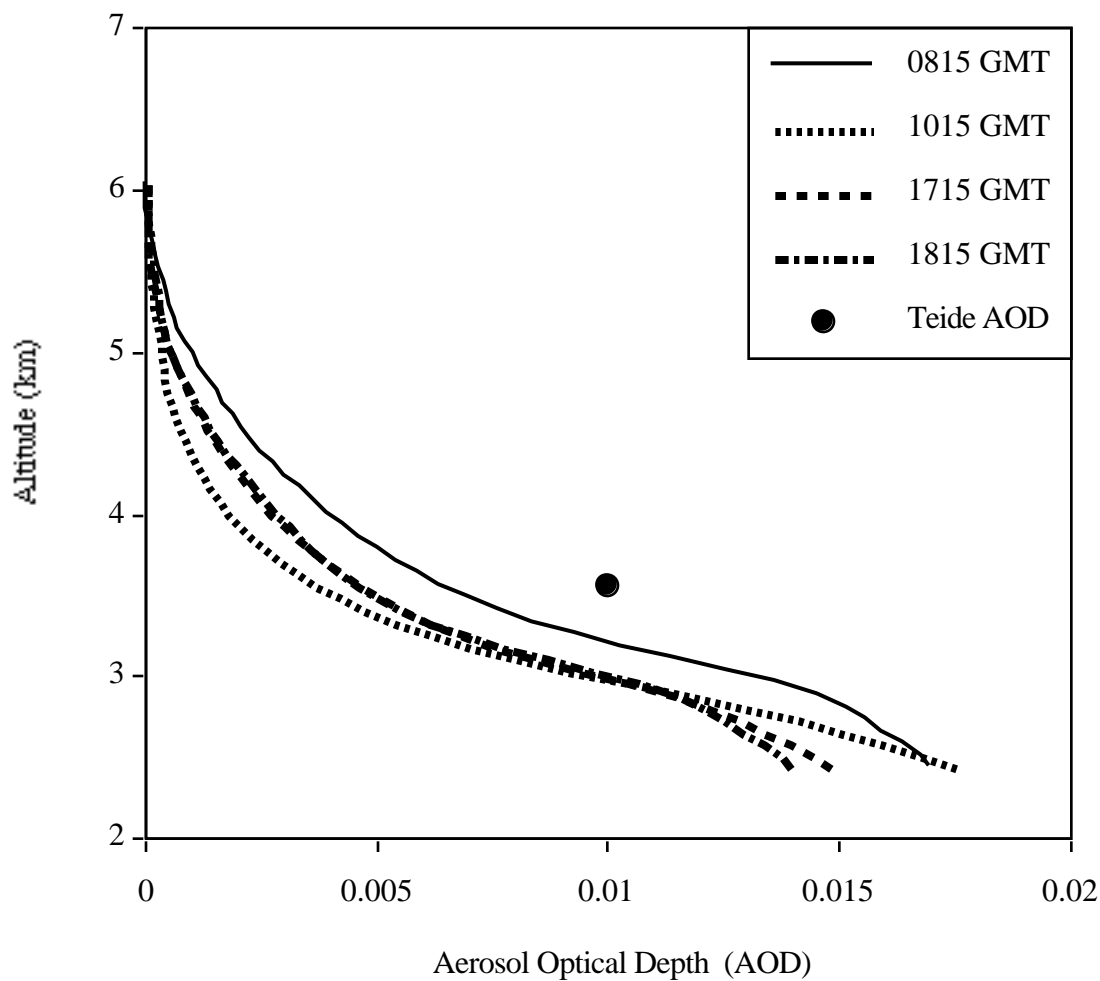


Figure 7b. Lidar aerosol optical depth (AOD) profiles at 08:15, 10:15, 17:15, and 18:15 GMT on June 29, 1997. The columnar AOD for each profile is 0.017, 0.018, 0.015, and 0.014 respectively. The calculated columnar backscatter-extinction ratios (1/sr) for each profile are 0.018, 0.038, 0.031, and 0.017 respectively. The average AOD measured by the Teide shadowband is also shown.

Figure 8

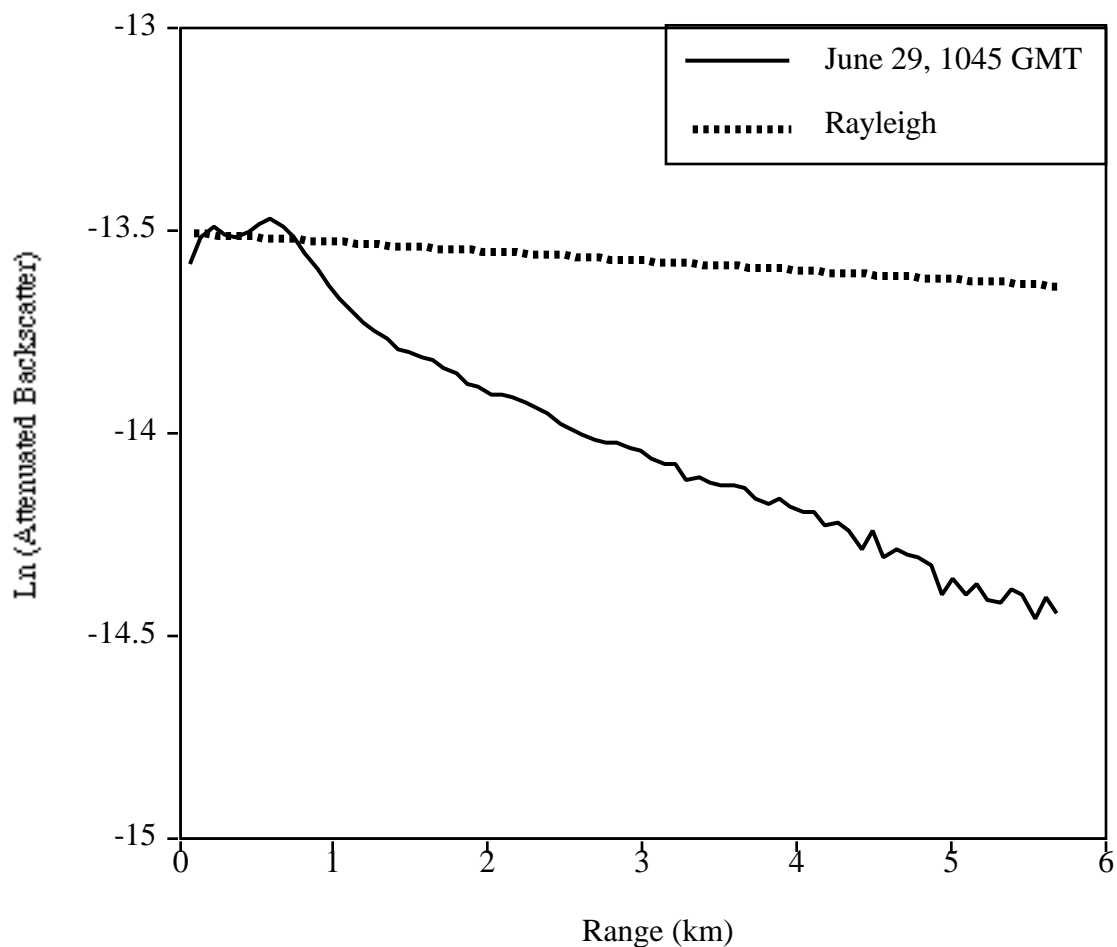


Figure 8. Horizontal lidar profiles of the natural logarithm of the attenuated backscatter coefficient, 1(m sr). A 15 minute average horizontal profile at 10:45 GMT on June 29 is shown along with a calculated Rayleigh horizontal profile for the IZO altitude.

Figure 9

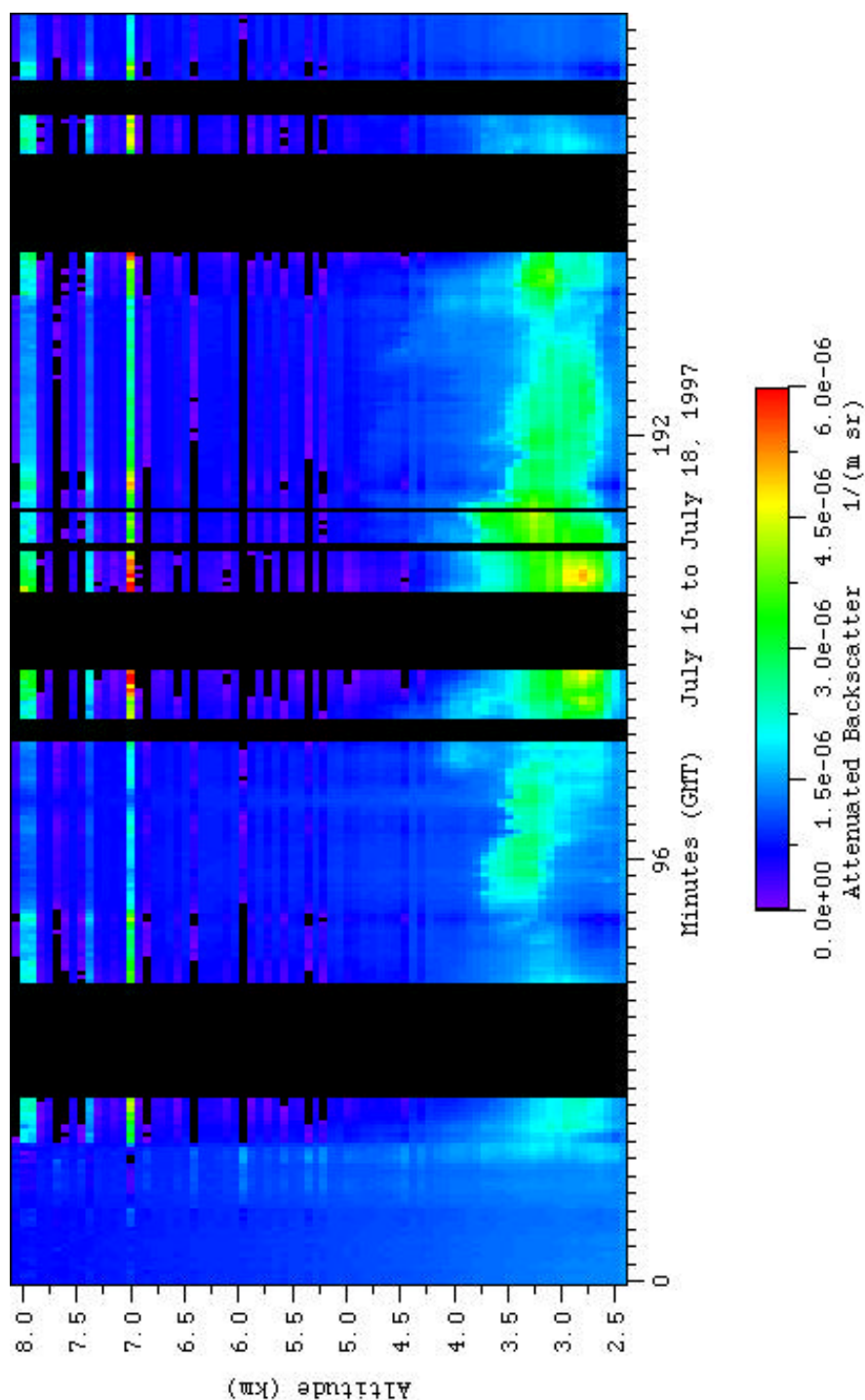


Figure 9. Three-day attenuated backscatter signal (ABS)  $(\text{m sr})^{-1}$  time series from July 16 through July 18, 1997. Each major tickmark separates the days, and each minor tickmark is one hour (GMT).



Figure 10

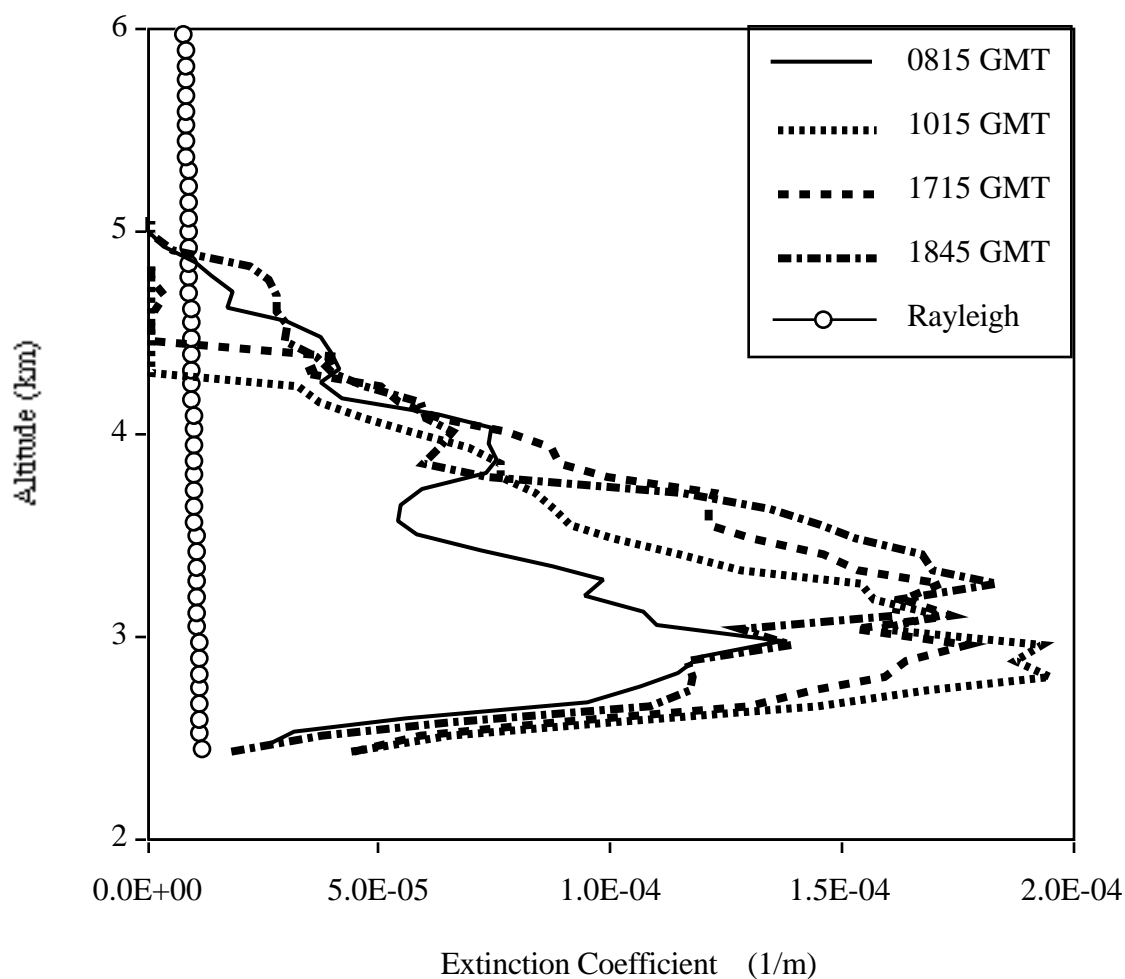


Figure 10. Lidar aerosol extinction coefficient ( $1/m$ ) profiles at 08:15, 10:15, 17:15, and 18:45 GMT on July 17, 1997. The columnar AOD for each profile is 0.161, 0.205, 0.226, and 0.217 respectively. The calculated columnar backscatter-extinction ratios ( $1/sr$ ) for each profile are 0.026, 0.048, 0.073, and 0.027 respectively. The Rayleigh extinction coefficient profile is shown for comparison.

Figure 11a

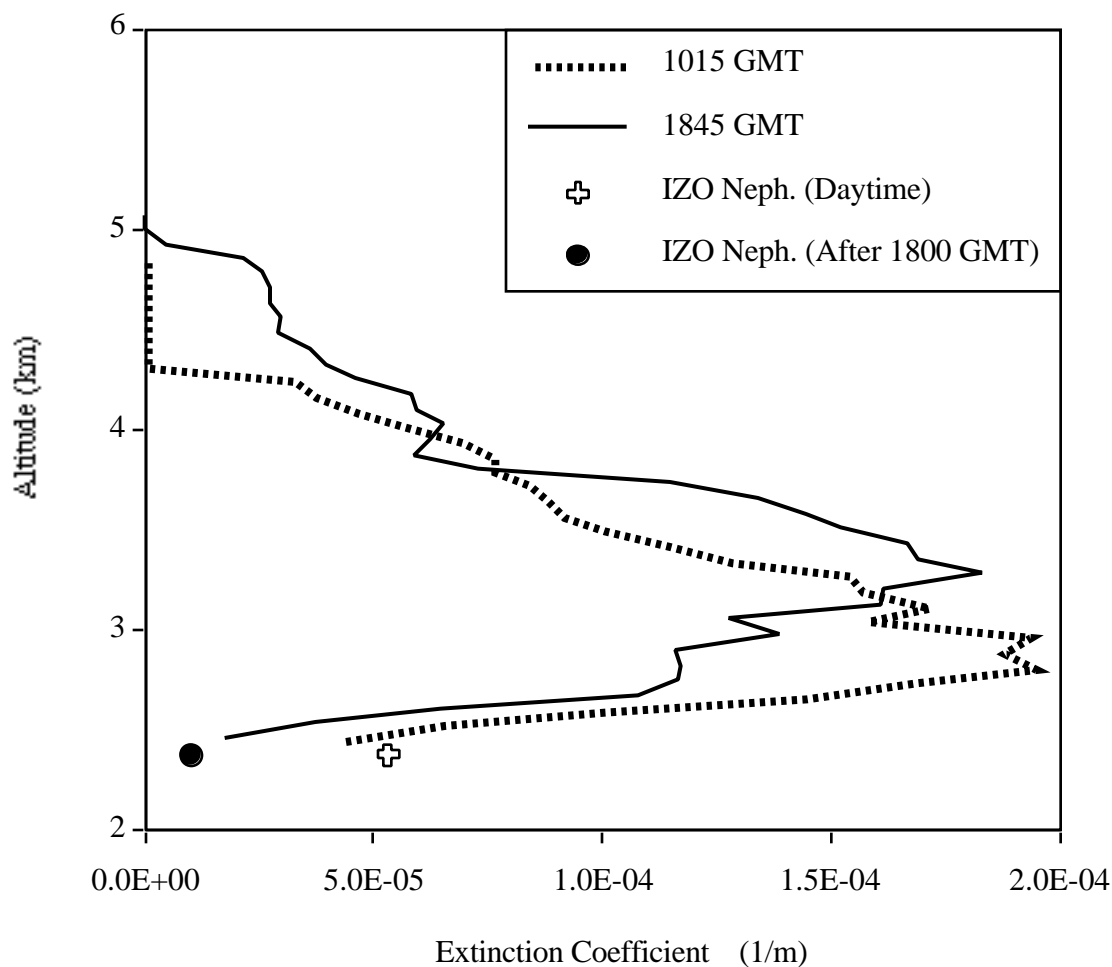


Figure 11a. Lidar aerosol extinction coefficient (1/m) profiles at 10:15 and 18:45 GMT on July 17, 1997. The columnar AOD for each profile is 0.205 and 0.217 respectively. The calculated columnar backscatter-extinction ratios (1/sr) for each profile are 0.048 and 0.027 respectively. The average aerosol extinction coefficients measured by the IZO nephelometer from 07:00 to 18:00 GMT (daytime) and after 18:00 GMT are also shown.

Figure 11b

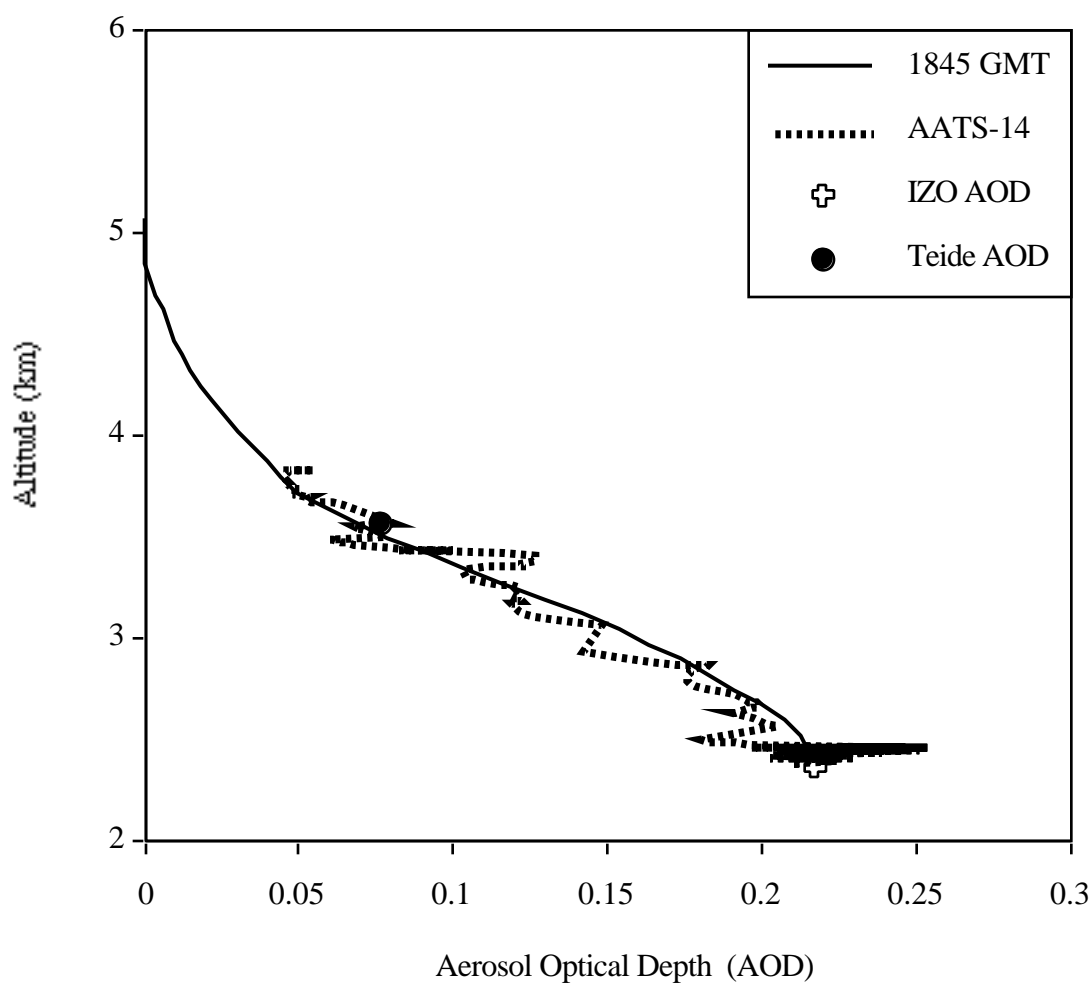


Figure 11b. Lidar aerosol optical depth (AOD) profile at 18:45 GMT on July 17, 1997. The columnar AOD is 0.217 and the calculated columnar backscatter-extinction ratio (1/sr) is 0.027. The AOD profile measured with AATS-14 from 18:30 to 18:45 GMT, and the AOD measured by the IZO cimel and the Teide shadowband, are also shown.

Figure 12

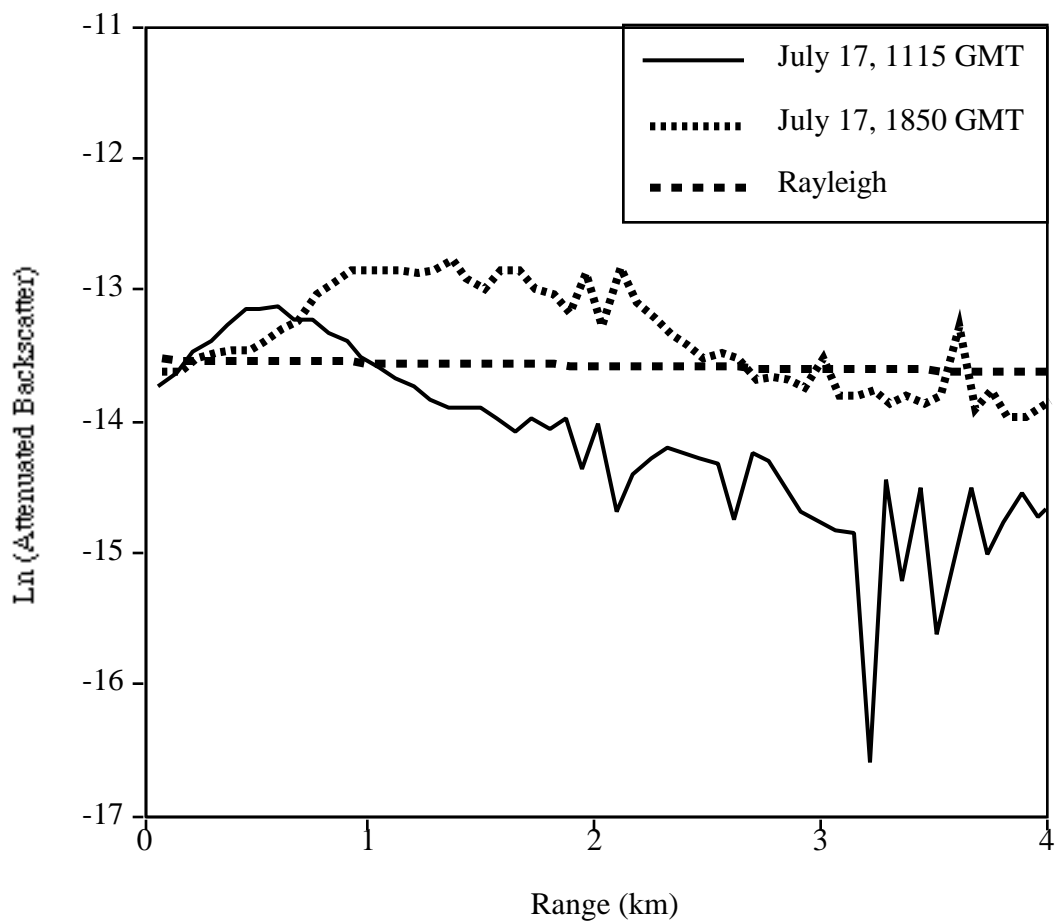


Figure 12. Horizontal lidar profiles of the natural logarithm of the attenuated backscatter coefficient,  $\ln(\text{m sr})$ . A 15 minute average horizontal profile at 11:15 GMT and a 5 minute average horizontal profile at 18:50 GMT on July 17 are shown along with a calculated Rayleigh horizontal profile for the IZO altitude.

Figure 13

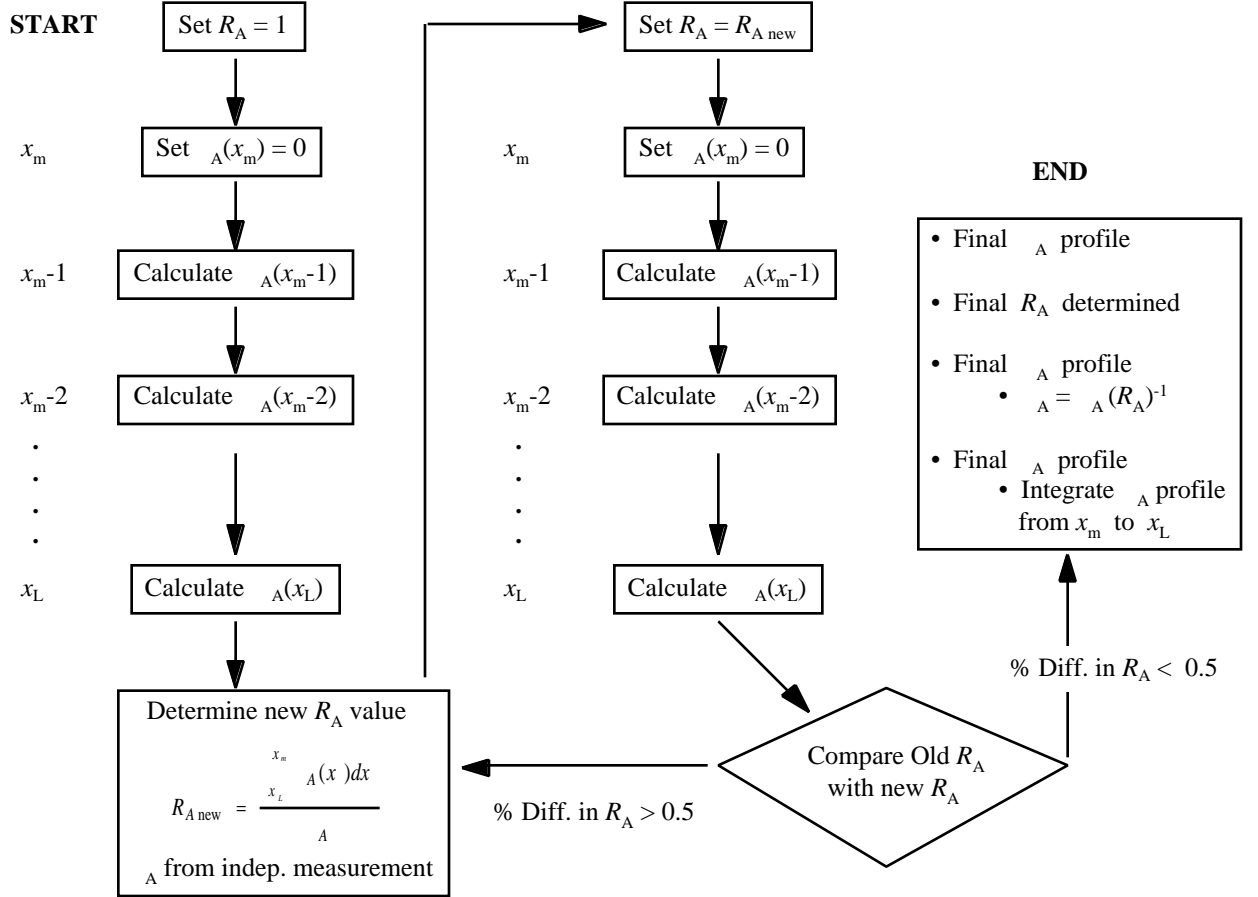


Figure 13. Schematic representation of the lidar inversion algorithm.